

Liquid Crystal Elastomer Lattices with Thermally Programmable Deformation via Multi-Material 3D Printing

Arda Kotikian, Audrey A. Watkins, Giovanni Bordiga, Andrew Spielberg, Zoey S. Davidson, Katia Bertoldi, and Jennifer A. Lewis*

An integrated design, modeling, and multi-material 3D printing platform for fabricating liquid crystal elastomer (LCE) lattices in both homogeneous and heterogeneous layouts with spatially programmable nematic director order and local composition is reported. Depending on their compositional topology, these lattices exhibit different reversible shape-morphing transformations upon cycling above and below their respective nematic-to-isotropic transition temperatures. Further, it is shown that there is good agreement between their experimentally observed deformation response and model predictions for all LCE lattice designs evaluated. Lastly, an inverse design model is established and the ability to print LCE lattices with the predicted deformation behavior is demonstrated. This work opens new avenues for creating architected LCE lattices that may find potential application in energy-dissipating structures, microfluidic pumping, mechanical logic, and soft robotics.

1. Introduction

Liquid crystal elastomers (LCEs) are stimuli responsive materials that hold promise for applications in soft robotics,^[1–3] artificial muscles,^[4–6] shape-shifting architectures,^[5,7] and tissue engineering.^[8] Main-chain LCEs are composed of elastomeric networks that contain rigid liquid crystalline moieties, known as mesogens, along their backbone. These stimuli-responsive materials actuate when heated above their nematic-to-isotropic transition temperature (T_{NI}),^[5–7] exposed to light,^[9,10] or exposed to

chemical gradients.^[11,12] By programming director alignment in the nematic state, LCEs can be produced that exhibit large, reversible contractility when cycled above and below their respective T_{NI} values.^[13,14] To date, several methods have emerged to program director alignment, including mechanical alignment that produces LCEs with large unidirectional contraction,^[3,6] command surfaces that yield thin films with a pixelated director field,^[5,7,15] magnetic alignment,^[11,16,17] and 3D printing^[18–22] to produce thick LCEs in arbitrary motifs. Of these methods, only direct ink writing (DIW), an extrusion-based 3D printing method, enables seamless integration of LCEs and other materials within origami-based robots,^[2,23] innervated LCE fibers,^[24] soft electronics,^[23–25] and shape-morphing textiles.^[26,27]

Despite these promising advances, the ability to create architected lattices composed of multiple LCE materials with varying T_{NI} remains challenging. These open architectures are composed of repeating unit cells, whose strut composition, size, and geometric layout drive their shape morphing and mechanical responses to external stimuli. The first demonstrations of shape-morphing LCE lattices consisted of orthogonally printed bilayers^[28] and square cellular architectures^[19] fabricated by DIW of main-chain LCE inks. More recently, 2D auxetic lattices with tunable Poisson's ratio have been produced by this method.^[21] In related work focused on side-chain and end-on LCEs, researchers have created 2D cellular architectures by using soft lithography to define their initial geometry coupled with an applied magnetic field to guide their director alignment^[29] or via electrowriting.^[30] However, in those methods, one produces periodic LCE lattices that are substrate-attached, which confines their shape morphing response. Emerging efforts are focused on generating 3D lattices using digital light projection (DLP).^[20] While those LCE lattices lack director alignment, they exhibit substantially higher energy dissipation under compressive loading than other commercially available photocurable elastomers. However, irrespective of their fabrication method, each of these previously reported LCE lattices is constructed from a single LCE with a specific T_{NI} .

Here, we report the design, modeling, and fabrication of soft architected lattices composed of multiple LCEs that exhibit programmable and predictable deformation sequences in response to heat. By directly printing multiple LCE inks with disparate actuation temperatures, we created triangular cellular lattices in

A. Kotikian, A. A. Watkins, G. Bordiga, A. Spielberg, Z. S. Davidson, K. Bertoldi, J. A. Lewis
 John A. Paulson School of Engineering and Applied Sciences
 Harvard University
 Cambridge, MA 02138, USA
 E-mail: jalewis@seas.harvard.edu

A. Kotikian, A. Spielberg, Z. S. Davidson, J. A. Lewis
 Wyss Institute for Biologically Inspired Engineering
 Harvard University
 Cambridge, MA 02138, USA

 The ORCID identification number(s) for the author(s) of this article can be found under <https://doi.org/10.1002/adma.202310743>

© 2024 The Authors. Advanced Materials published by Wiley-VCH GmbH. This is an open access article under the terms of the [Creative Commons Attribution-NonCommercial-NoDerivs](#) License, which permits use and distribution in any medium, provided the original work is properly cited, the use is non-commercial and no modifications or adaptations are made.

DOI: 10.1002/adma.202310743

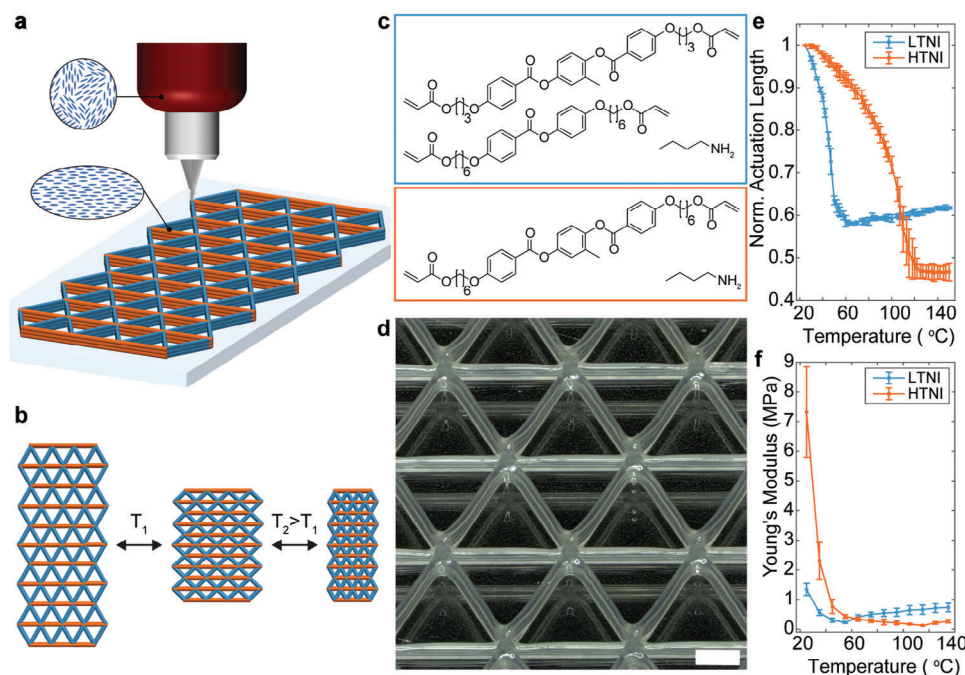


Figure 1. Printing LCE lattices. a) Schematic illustration of HOT-DIW of a triangular heterogeneous lattice composed of two LCE inks with different nematic-to-isotropic transition temperatures (LTNI and HTNI), where each director is aligned along the print path. Insets depict alignment of LCE ink morphology from polydomain (in ink reservoir) to aligned after printing. b) Schematic illustration of the sequential deformation observed upon heating a heterogeneous LCE lattice, where individual struts contract upon heating above their respective T_{NI} values. c) Chemical composition of the LTNI (blue) and HTNI (orange) oligomeric inks. d) Optical image (tilted view) of a heterogeneous LCE lattice with a printed unit cell composition that corresponds to the schematic in b) (scale bar = 1 mm). e) Normalized length of unbiased actuation of uniaxially aligned, 3D printed LTNI and HTNI LCE thick films as a function of temperature. f) Young's modulus values measured for uniaxially aligned, 3D printed LTNI and HTNI LCE thick films as a function of temperature. Error bars indicate standard deviation ($n \geq 3$).

which each strut is composed of a given LCE with director alignment parallel to the strut direction (Figure 1). As controls, we first fabricate homogenous triangular lattices with low T_{NI} (LTNI) or high T_{NI} (HTNI) LCE struts, characterize their deformation response and stiffness as a function of temperature, and then use these data to validate our simplified spring model (see SI). Next, we design, fabricate, and characterize heterogeneous triangular lattices (Figure 1a). By co-printing two LCEs with disparate T_{NI} values, we encode varying deformation modes in lattices with the same global geometry, yet different localized compositional topology that are thermally triggered on demand. These soft architected lattices exhibit shear-induced configurations. We also generated nonperiodic LCE lattices that exhibit more complex shape morphing sequences upon heating. Last, we introduce an inverse-design framework to automatically discover binary distributions of LTNI and HTNI LCE struts that encode transformations between multiple target shapes upon monotonic heating.

2. Results and Discussion

Homogeneous and heterogeneous LCE lattices are fabricated by printing LTNI and/or HTNI LCE inks via high operating temperature (HOT) DIW.^[19,28] We focused on triangular lattices printed in six unit cell variations with varying strut composition. LTNI and HTNI LCE inks are printed at 31 °C and 50 °C, in their respective nematic phases, where each ink exhibits shear thinning behavior and shear-induced director alignment (Figure 1a;

Figure S1, Supporting Information). Each lattice strut is comprised of one of these LCEs with disparate thermal response, such that lattice deformation configurations upon heating can be topologically programmed (Figure 1b). Both LCE inks are composed of acrylate-terminated oligomers that undergo acrylate polymerization via UV curing after the inks exit the nozzle. The LTNI ink contains two liquid crystalline mesogens with different aromatic content to reduce liquid crystallinity^[28] and, hence, its lower T_{NI} value,^[29] while the HTNI ink is composed of a single mesogen that gives rise to a high T_{NI} value^[5,19] (Figure 1c). The LTNI ink also contains two spacer lengths to suppress smectic phase formation.^[30] Each triangular lattice is printed in four layer motifs with strut diameters of 250 μm (i.e., a single ink filament wide), which exhibit strong intra- and inter-LCE ink crosslinking between each layer (Figure 1d; Figure S2, Supporting Information). The printed LCE struts exhibit repeatable contraction along the print direction when each homogeneous lattice is heated above its respective minimum actuation temperature of 65 °C (LTNI struts) and 125 °C (HTNI struts). Normalized contractile actuation lengths of 0.581 ± 0.004 and 0.468 ± 0.017 , respectively, are measured for uniaxially aligned LCE thick films, which served as 3D printed controls (Figure 1e). The pronounced difference in the onset of their temperature-dependent response of heterogeneous LCE lattices is essential for the sequential actuation of LTNI and HTNI struts, which gives rise to programmable shape morphing and mechanics.^[31] Under ambient conditions, HTNI LCE struts exhibit a roughly five-fold difference in their Young's

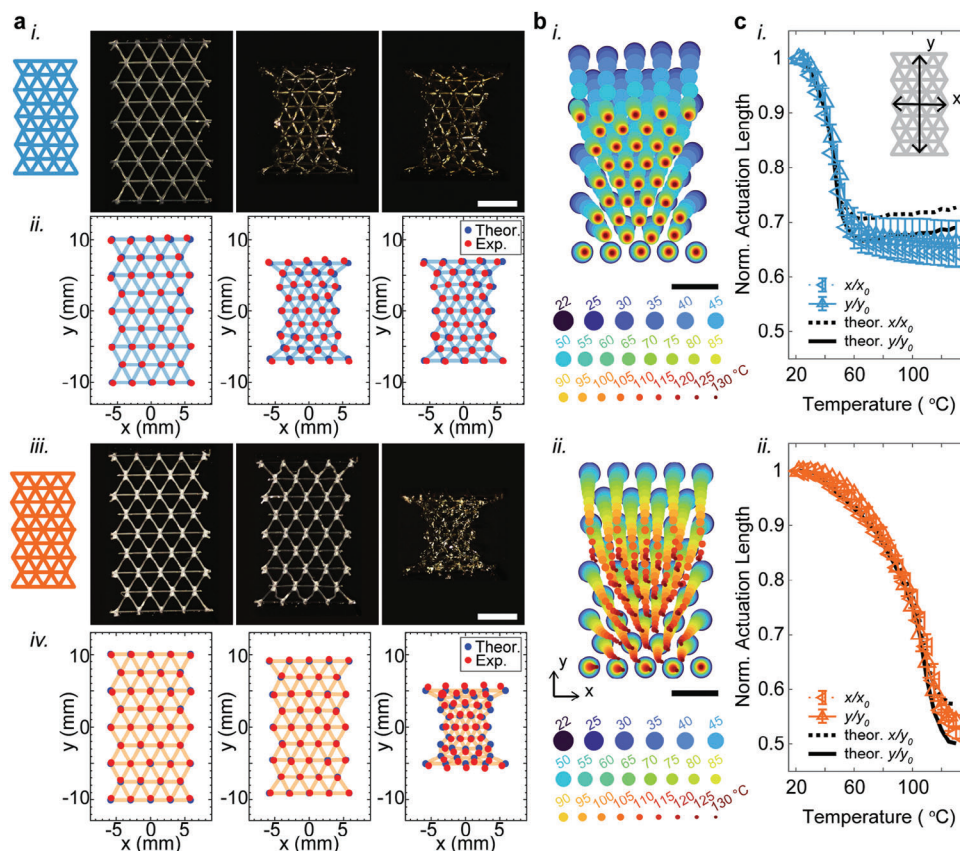


Figure 2. Homogenous LCE lattices. a) Representative images and corresponding nodal representations of homogeneous LTNI (i-ii) and HTNI (iii-iv) lattices at 22 °C (left), 70 °C (middle), and 130 °C (right), where both representative nodes (red) and modeled deformation topologies (blue) are shown. b) Experimentally observed node positions as a function of temperature for pure (i) LTNI and (ii) HTNI lattices (scale bars = 5 mm). c) Average normalized dimensions in x and y directions measured for (i) LTNI and (ii) HTNI lattices as a function of temperature, where x and y dimensions are normalized by their initial dimensions at ambient conditions. Dimensions extracted from the model are overlaid. Error bars indicate standard deviation (n = 3).

modulus relative to LTNI LCE struts, while they exhibit similar values near 60 °C (Figure 1f) since their stiffness decreases markedly upon heating.

As a benchmark, we first printed homogenous triangular lattices composed solely of LTNI or HTNI LCE struts with overall dimensions of $11.5 \times 20 \times 0.5 \text{ mm}^3$ and captured both free (left and right) and constrained (top and bottom) edge effects as a function of temperature (Figure 2). Both LTNI (Figure 2a, i-ii) and HTNI (Figure 2a, iii-iv) lattices undergo homogeneous deformation upon heating, akin to their unidirectional aligned, thick film counterparts. Both lattices exhibit a large contractile response along the printed strut directions and an optical transition from opaque to clear that arises due to their respective nematic-to-isotropic phase transitions. Each lattice adopts an hourglass-like configuration above their respective T_{NI} due to their constrained top and bottom edges. We then quantified the local actuation of struts and global deformation of both LCE lattices by measuring their node displacement (Figure 2b; Figures S3 and S4, Supporting Information) as well as overall shape evolution (Figure 2c) as a function of temperature. In the latter case, we report their normalized actuation width defined by the average lattice width, x , at a given temperature divided by their initial width (x_0), mea-

sured along the x-axis for the center row of struts) under ambient conditions and their normalized actuation length (y) divided their initial length (y_0). In both cases, there is marginally higher contraction along the x direction due to their triangular lattice geometry. Not surprisingly, the resulting director alignment and, hence, observed global shape change is slightly lower for these homogeneous LCE lattices, which have more complex print paths compared to uniaxially aligned, thick films of the same composition.

The deformation of homogenous triangular lattices is nicely captured using a model composed of a network of thermo-elastic springs with temperature-dependent material properties.^[1] The strain energy of each strut is assumed to be

$$\psi = \frac{1}{2} E(T) A_0 l_0 \left(\frac{\lambda}{1 + \alpha [\lambda_T(T) - 1]} - 1 \right)^2 \quad (1)$$

where λ is the stretch (defined as the ratio between the length of the strut at temperature T and at room temperature) and $A_0 = 0.0625 \text{ mm}^2$ and $l_0 = 2.9 \text{ mm}$ are the cross-sectional area and length of each strut at room temperature. Moreover, $E(T)$

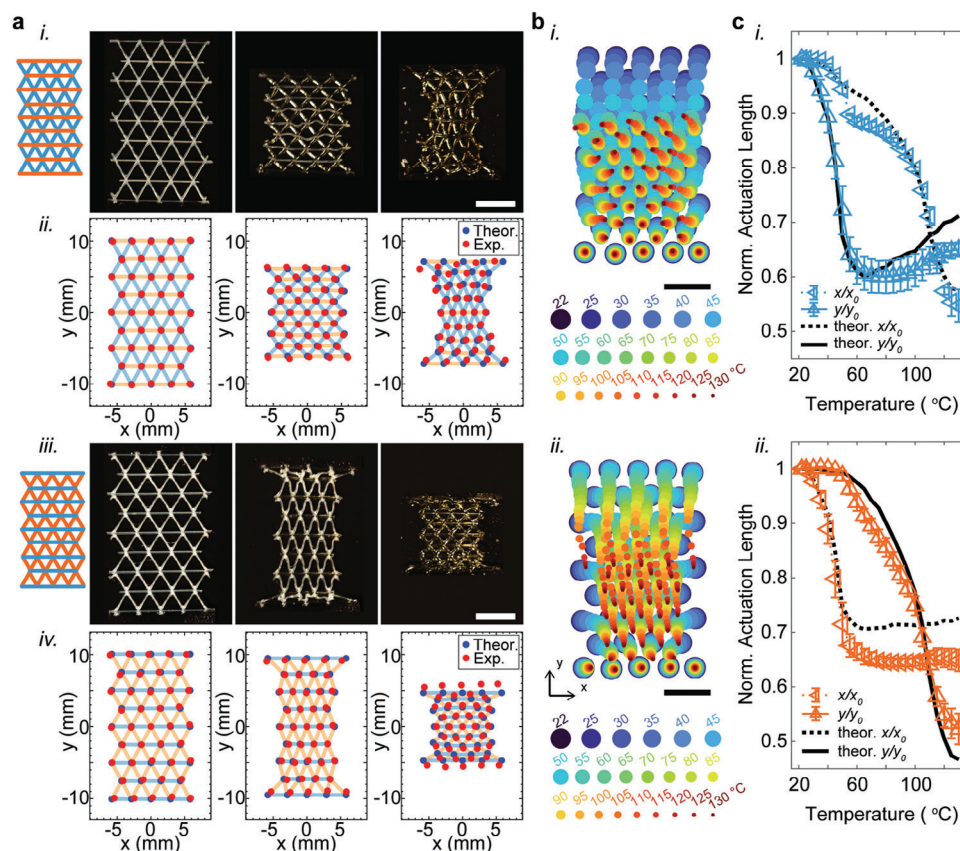


Figure 3. Heterogeneous LCE lattices with fixed horizontal and diagonal strut compositions. a) Representative images and corresponding nodal representations of (i-ii) LTNI-HTNI₀ and (iii-iv) HTNI-LTNI₀ lattices at 22 °C (left), 70 °C (middle), and 130 °C (right), where both representative nodes (red) and modeled deformation topologies (blue) are shown. b) Experimentally observed node positions as a function of temperature for representative (i) LTNI-HTNI₀ and (ii) HTNI-LTNI₀ lattices (scale bars = 5 mm). c) Average normalized dimensions in x and y directions measured for (i) LTNI-HTNI₀ and (ii) HTNI-LTNI₀ lattices at discrete temperatures, where x and y dimensions are normalized by initial dimensions at ambient conditions. Dimensions extracted from the model are overlaid. Error bars indicate standard deviation (n = 3).

and $\lambda_T(T)$ are the experimentally measured Young's modulus (Figure 1f) and stretch values (Figure 1e) of the LCE material as a function of the temperature T , respectively. Note, that the parameter α is introduced to account for lower director orientational order at each node within the printed LCE lattices and we chose $\alpha = 0.7$ and $\alpha = 0.8$ for LTNI and HTNI LCE, respectively. As shown in Figure 2, the numerically predicted deformation of both LTNI and HTNI LCE lattices are in good agreement with their experimental observation (see also Figures S5 and S6, Supporting Information), with modest discrepancy arising due to manufacturing defects (e.g., over-extrusion of each LCE ink at the initiation of each strut). In the future, optimized print path planning^[32] that minimizes starts/stops during the construction of architected LCE lattices could be deployed to reduce such defects.

To increase lattice complexity, we used multi-material DIW to fabricate heterogeneous triangular lattices composed of both LTNI and HTNI LCE struts. Specifically, these heterogeneous LCE lattices possess either diagonal LTNI struts and horizontal HTNI struts (henceforth referred to as LTNI-HTNI₀) or the opposite motif with diagonal HTNI struts and horizontal LTNI struts (HTNI-LTNI₀) (Figure 3). Upon heating the heterogeneous LCE

lattices, the LTNI struts contract first followed by the HTNI struts inducing sequential changes in their global shape. For example, the LTNI-HTNI₀ lattices morph between their initial equilateral triangular cells to obtuse isosceles triangular cells upon heating above the LTNI actuation temperature of 65 °C due to contractions of their diagonal struts (Figure 3a, i-ii). When further heated above the HTNI actuation temperature of 125 °C, the lattices adopt an hourglass-like configuration akin to their homogeneous counterparts. The lattice spring model captures the experimentally observed nodal deformation across the full temperature range (Figure 3b-c, i; Figure S7, Supporting Information). These LTNI-HTNI₀ lattices exhibit most of their initial deformation along the y axis, followed by contraction of the HTNI struts along the x axis at higher temperatures, which gives rise to modest buckling of those struts to accommodate large deformations near their constrained (top-bottom) boundaries. While our model does not account those effects, it does capture their overall deformation with high fidelity. By contrast, when HTNI-LTNI₀ lattices are heated over the same temperature range, the LTNI struts first contract laterally along the x-axis leading to elongated unit cells, followed by the subsequent contraction of HTNI struts at higher temperatures to produce a final, hourglass shape (Figure 3a, iii-iv;

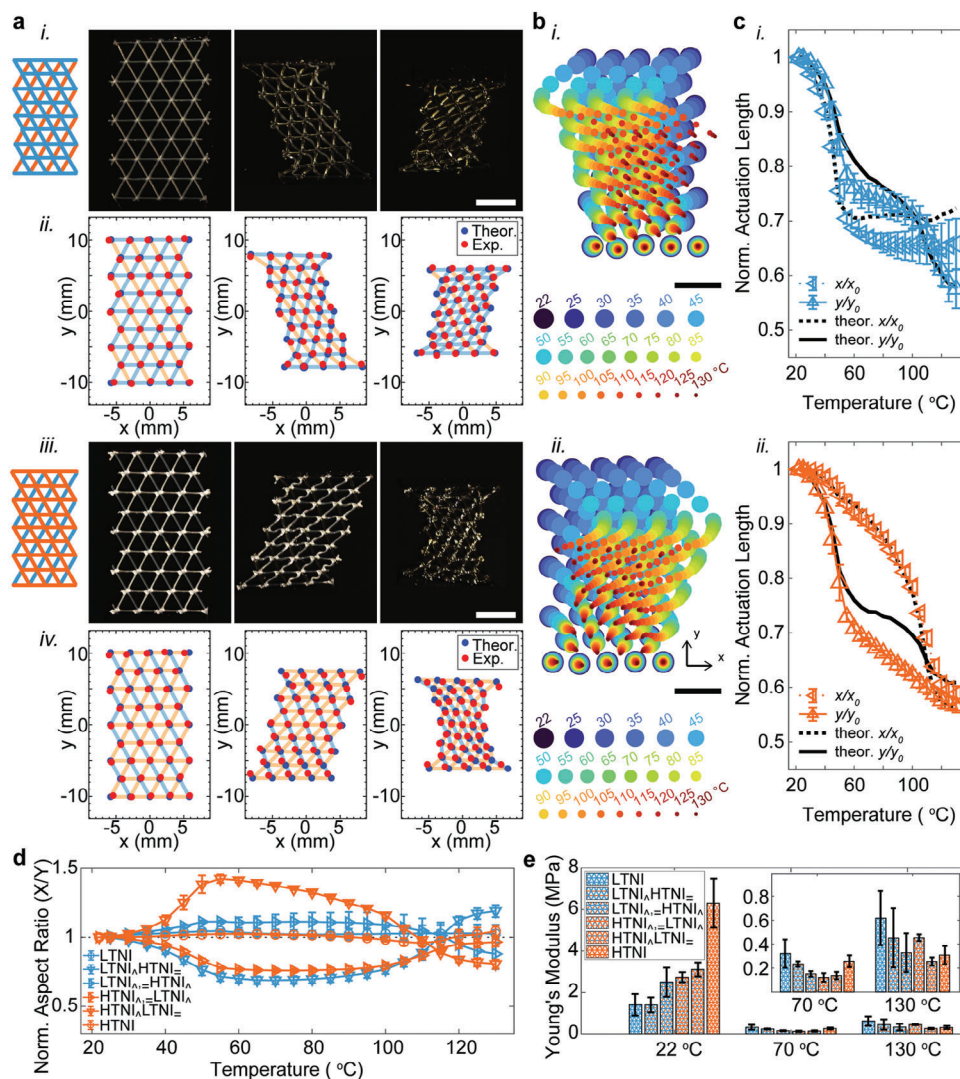


Figure 4. Heterogeneous LCE lattices with programmable horizontal and diagonal strut compositions. a) Representative images and corresponding nodal representations of (i-ii) $\text{LTNI}_{\perp} = \text{HTNI}_{\perp}$ and (iii-iv) $\text{HTNI}_{\perp} = \text{LTNI}_{\perp}$ lattices at 22 °C (left), 70 °C (middle), and 130 °C (right), where both representative nodes (red) and modeled deformation topologies (blue) are shown. b) Experimentally observed node positions as a function of temperature for representative (i) $\text{LTNI}_{\perp} = \text{HTNI}_{\perp}$ and (ii) $\text{HTNI}_{\perp} = \text{LTNI}_{\perp}$ lattices (scale bars = 5 mm). c) Average normalized dimensions in x and y directions measured for (i) $\text{LTNI}_{\perp} = \text{HTNI}_{\perp}$ and (ii) $\text{HTNI}_{\perp} = \text{LTNI}_{\perp}$ lattices at discrete temperatures, where x and y dimensions are normalized by initial dimensions at ambient conditions. Dimensions extracted from the model are overlaid. d) Normalized aspect ratio, normalized to aspect ratio at ambient conditions for all six periodic lattices at discrete temperatures. e) Young's modulus of all six types of periodic lattices at discrete temperatures. Error bars indicate standard deviation ($n = 3$).

Figure S8, Supporting Information). Once again, our model accurately captures the shape evolution of those lattices; However, it slightly underestimates LTNI LCE strut contractility likely due to in-plane stress imposed by the HTNI LCE strut contraction. Despite their arrangement along the diagonal directions, the HTNI LCE struts induce substantial strain in the y direction relative to the x direction within the $\text{HTNI}_{\perp}\text{LTNI}_{\perp}$ lattices at elevated temperatures (Figure 3c, ii).

To program different shape morphing responses, we printed heterogeneous triangular LCE lattices composed of a LTNI diagonal strut, a HTNI diagonal strut, and another strut of varying composition, i.e., lattices possessing either $\text{LTNI}_{\perp} = \text{HTNI}_{\perp}$ or $\text{HTNI}_{\perp} = \text{LTNI}_{\perp}$ unit cells (Figure 4). Upon initial heating the

$\text{LTNI}_{\perp} = \text{HTNI}_{\perp}$ lattices, the dual LTNI struts in each unit cell contract giving rise to a shear-induced deformation (Figure 4a, i-ii). Despite some buckling of HTNI struts near the constrained (top-bottom) edges, our simple spring model effectively captures the observed lattice deformation upon heating (Figure 4b-c, i). At intermediate temperatures, these heterogeneous LCE lattice dimensions change nearly isotropically, since the LTNI struts are arranged in both horizontal and diagonal directions. However, upon heating above the actuation temperature of the HTNI struts, these lattices adopt a second shearing configuration that is mirror opposite, albeit with reduced global dimensions, due to strain mismatch of the respective LCE struts (Figure 4a-b, ii). Their respective strain mismatch coupled with their

compositional topology results in greater contraction in the y direction than the x direction for LTNI \rightarrow HTNI lattices, akin to that observed for HTNI-LTNI lattices (Figure 4c,i). Conversely, upon heating HTNI \rightarrow LTNI lattices, the LTNI LCE struts contract first approximating a sheared rectangle with the long edge $\approx 60^\circ$ from the initial LTNI strut direction prior to forming an hourglass-like shape similar to HTNI lattices (Figure 4a,iii-iv). The deformation of these heterogeneous lattices is also well predicted by our simple spring model (Figure 4c; Figures S9 and S10, Supporting Information). In this case, the HTNI \rightarrow LTNI lattices deform primarily in the x direction at moderate temperatures due to the orientation of the LTNI struts, followed by a slightly larger contraction in the y direction relative to the x direction at elevated temperatures. Again, due to the strain mismatches between both LCEs and their constrained edges, there is a minimal amount of out-of-plane deformation observed at elevated temperatures.

By determining their normalized aspect ratios at discrete temperatures, we directly compared the responses of the six unit cell types explored to guide the design of active LCE lattices in new target motifs (Figure 4d). While homogenous LCE lattices maintained relatively constant aspect ratio as they deformed, the heterogeneous LTNI- \rightarrow HTNI and HTNI-LTNI lattices exhibited pronounced variations in their aspect ratios, with greater deformations in either y or x directions, respectively, at moderate temperatures and the inverse at elevated temperatures. By contrast, the more complex LTNI \rightarrow HTNI and HTNI \rightarrow LTNI lattices have similar trends in aspect ratio as HTNI- \rightarrow HTNI and LTNI-LTNI lattices, respectively. Notably, for all six unit cell motifs, their overall shapes and normalized aspect ratios are similar to one another at $\approx 110^\circ\text{C}$, where LTNI and HTNI strut strains are near identical. As expected, their complex shape morphing response, which arises from their disparate T_{NI} and maximum actuation strains of the LTNI and HTNI struts, can be reversed when slowly cooled to room temperature (Figure S11, Supporting Information). Under ambient conditions, lattices with higher fraction of HTNI struts arranged in diagonal topologies exhibited considerably higher Young's moduli due to their intrinsic LCE stiffnesses and geometry (Figure 4e; Figure S12, Supporting Information). The opposite is observed for heterogeneous LCE lattices composed of a higher fraction of LTNI struts. At moderate temperatures, their lattice moduli are similar, while LTNI homogenous lattices are considerably stiffer at elevated temperatures.

Importantly, our integrated design, fabrication, and modeling approach can be extended to create arbitrary heterogeneous architectures. As an exemplar, we designed a slender architecture with a bilayer topology that transforms from a long rectangle to a bent configuration at moderate temperatures, returns to a smaller rectangle, then bends with opposite curvature at elevated temperatures (Figure 5a; Figures S13a and S14 and Movie S1, Supporting Information). Bimodal bending arises due to the disparate strains of the LTNI and HTNI struts, which may lead to their applications as active hinges in origami-based soft robots and other devices. Next, we printed a large nonperiodic rectangular lattice that exhibits four distinct segments consisting of the HTNI \rightarrow LTNI lattice and its mirror image tessellated in one direction (Figure 5b; Figures S13b and S15 and Movie S2, Support-

ing Information). This pattern results in a zig-zag deformation initiated by the shearing modes of the underlying lattice segments at moderate temperatures. Subsequently, it reverts to a smaller rectangle and ultimately transforms into mirrored zig-zag patterns at elevated temperatures (Figure 4a,iii-iv). Notably, our model accurately predicts the deformation of both architectures (Figures 5a,b).

Our combined experimental and numerical results indicate that by varying the arrangement of LTNI and HTNI struts within a triangular lattice, qualitatively different deformation sequences can be achieved upon changes in temperature. However, for practical applications it is very important to identify architectures resulting in specific temperature-driven shape transformations. Such problems can be expressed as a multi-objective optimization problem whose solution is the arrangement of LTNI and HTNI struts that minimize a prescribed objective function. Our inverse-design framework is based on the SIMP material interpolation^[33] between the thermo-elastic properties (actuation strain and Young's modulus) of LTNI and HTNI LCE materials. In particular, a continuous phase variable $z \in [0,1]$ is introduced to continuously interpolate between LTNI ($z = 1$) and HTNI ($z = 0$). To identify domains leading to a sequence of target shapes at distinct temperatures, we minimize the cost function

$$J_{\text{tot}} = \sum w_i J_i \quad (2)$$

Where J_i quantifies the distance between the i^{th} target shape at T_i and the simulated configuration at the corresponding temperature and $w_i \in [0,1]$ is the weighting variable for the i^{th} objective. The cost function of Equation 2 is minimized using the Method of Moving Asymptotes (MMA)^[34] with gradient information provided by our JAX-based differentiable simulations (see Supporting Information for additional details). To demonstrate our approach, we focus on two distinct target shapes at $T = 70^\circ\text{C}$ and $T = 130^\circ\text{C}$ and search for an optimal solution for which $J_1 \approx J_2$. In the first example we identify arrangement of LTNI and HTNI struts that make the centerline of a slender lattice domain at $T = 22^\circ\text{C}$ transform to a sinusoid at $T = 70^\circ\text{C}$ and then to an inverted-sinusoid at $T = 130^\circ\text{C}$. The optimal design is identified choosing $w_1 = w_2 = 0.5$ which gives comparable performance for both target shapes. Figure 5c illustrates the good agreement observed among the target, simulated, and experimentally deformed configurations, affirming the validity of our inverse design framework. Subsequently, we explore a lattice domain initially shaped as a square at $T = 22^\circ\text{C}$, with its boundary transforming into a circle at $T = 70^\circ\text{C}$ and further into a 4-pointed star at $T = 130^\circ\text{C}$. To systematically explore the Pareto front for this multi-objective problem, we vary w_1 within $[0, 1]$ while setting $w_2 = 1 - w_1$. The optimal solution, identified with $w_1 = 0.93$ and $w_2 = 0.07$, equally minimizes both J_1 and J_2 . (Figure S20a, Supporting Information). Testing this optimal design reveals consistent agreement between experiments and simulations (Figure 5d; Movie S3, Supporting Information). Taken together, these results demonstrate that the integration of inverse design and additive manufacturing of lattices consisting of multiple LCE with disparate actuation temperatures enables the realization of programmable sequences of target shape transformations that can be triggered by monotonic temperature changes.

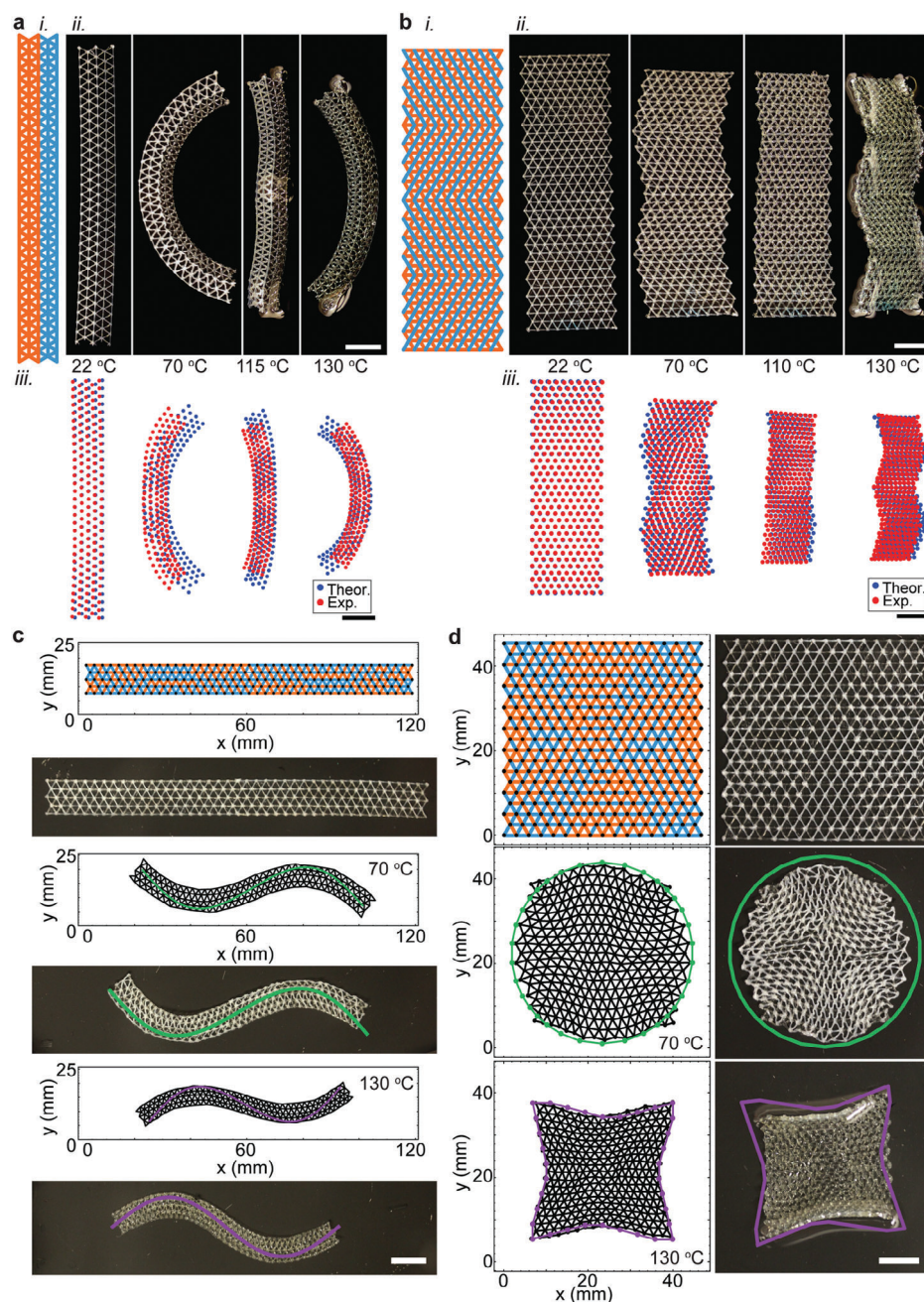


Figure 5. Segmented heterogeneous LCE lattices via inverse design. a) (i) Schematic representation of a bilayer heterogeneous lattices composed of LTNI (blue) bottom layer and HTNI (orange) top layer as a function of temperature. (ii) Corresponding images of a representative bilayer lattice and (iii) experimentally observed (red) and modeled (blue) lattice node positions at 22, 70, 115, and 130 °C (top to bottom). b) (i) Schematic representation of a complex heterogeneous lattices composed of four segments with varying LTNI (blue) and HTNI (orange) unit cell configurations. (ii) Corresponding images of a representative segmented lattice and (iii) experimentally observed (red) and modeled (blue) lattice node positions at 22, 70, 110, and 130 °C (top to bottom). Simulated inversely designed topology composed of LTNI (blue) and HTNI (orange) struts to achieve green and purple configurations at 70 and 130 °C, respectively, where black denotes modeled deformation and the corresponding experimental data for c) alternating curvature and d) multi-shape lattices (scale bars = 10 mm).

3. Conclusion

In summary, we have fabricated homogeneous and heterogeneous LCE lattices with triangular unit cells with six, compositionally distinct, unit cells. We established an integrated de-

sign, modeling, and multi-material 3D printing platform to create both period and nonperiodic architectures that exhibit large, programmable deformations. There was good agreement between model predictions and their experimentally observed shape transformation upon heating. We then implemented an

inverse design framework to create soft architected lattices capable of encoding transformations between various target shapes during monotonic heating. We envision that this framework can be extended to myriad LCE lattice designs with varying strut composition and multifunctional stimuli-responsive behavior for applications, such as temperature-dependent fluidic logic, reconfigurable electronics (e.g., patch antennas), and soft robotics with untethered sequential movement and programmable mechanics.

4. Experimental Section

Materials: The LTNI ink was prepared using an aza-michael addition. A 1:1 molar ratio of 1,4-bis-[4-(3-acryloyloxypropyloxy)benzoyloxy]-2-methylbenzene (Wilshire Technologies Inc.) and 4-(6-(acryloyloxy)hexyloxy)phenyl 4-(6-(acryloyloxy)hexyloxy)benzoate (Synthon) with 0.2 wt.% butylated hydroxytoluene (Fisher Scientific) was combined by heating to 100 °C and stirring. Next, 2 wt.% Irgacure 651 (BASF) and n-butylamine (Sigma-Aldrich) were added to the mixture such that the molar ratio of mesogen acrylates to amine is 1.1:1, and the reaction was stirred at 100 °C for 18 h. The HTNI ink was also prepared using an aza-michael addition, as reported previously.^[2,24] A 1.1:1 molar ratio of 1,4-bis-[4-(6-acryloyloxyhexyloxy)benzoyloxy]-2-methylbenzene (Wilshire Technologies Inc.) and n-butylamine (Sigma-Aldrich) were combined with 0.2 wt.% butylated hydroxytoluene (Fisher Scientific), and 2 wt.% Irgacure 651 (BASF), then stirred at 105 °C for 18 h. The inks were transferred to custom 3cc stainless-steel syringe barrels prior to printing.

Ink Rheology: The rheological properties of both LCE inks were measured on a stress-controlled shear rheometer (Discovery Hybrid Rheometer, HR-20, TA Instruments). Viscosity measurements were carried out using an 8 mm steel Peltier plate geometry with 500 μ m gap and applied shear rate of 0.001 to 100 s^{-1} at the inks' respective printing temperatures. The T_{NI} values of each ink were estimated from peaks of a temperature sweep on the rheometer with 20 mm steel Peltier plate geometry and 500 μ m gap. Inks were sheared at 1 Hz frequency from 20–150 °C with 5 Pa stress (HTNI LCE ink) or from 15–100 °C with 1% strain (LTNI ink) at a temperature ramp rate of 10 °C min^{-1} . Prior to all tests, the inks were heated above T_{NI} to erase any loading effects.

Multi-Material Printing: LCE lattices were printed using a multi-material 3D printer (customized ABG 10 000, Aerotech Inc.) or custom-built, three-axis motion-controlled stage (Aerotech Inc.) equipped with on-the-fly UV crosslinking at ≈ 7 mW cm^{-2} intensity (Omnicure, S2000). LCE inks are extruded through 250 μ m stainless-steel nozzles (TecDia, ARQUE-2535) by applying pressure (Ultimus V, Nordson EFD) via 3cc high pressure adapter (Nordson EFD) at 31 °C and 50 °C for LTNI and HTNI inks, respectively. Temperature control was achieved via a custom HOT-DIW printhead, as reported previously.^[2] The LCE inks were printed with print height of 0.125 mm, spacing of 0.125 mm for LCE test strips, average pressure of 525 psi, average speed of 3 mm s^{-1} or 28 mm s^{-1} for LTNI and HTNI inks, respectively, and print temperature of 31 °C and 50 °C for LTNI and HTNI inks, respectively.

All triangular LCE lattices were printed with a unit cell edge length of 2.887 mm, thickness of 0.5 mm, and overall height of 2.5 mm, except for those shown in Figure 5b, which were printed with thickness of 0.25 mm. Periodic lattices each contained 8×4 triangle unit cells of active area. Periodic lattices were printed with at least one additional row on both ends and manually infilled with adhesive material (Norland Optical Adhesive, NOA 68) to constrain their actuation at their top and bottom surfaces. The adhesive material was crosslinked by exposing it to UV light (≈ 10 mW cm^{-2} , Omnicure, S2000) for at least 10 min. This material was painted black for all images taken on a black background (Figures 2–4). Large triangular lattices were printed and then trimmed to 8×4 unit cells. The printing conditions and toolpath were generated using a custom script with a Python G-code generator (MeCode). After printing, LCE samples were further crosslinked with UV exposure of >30 min on each side at ≈ 4 –14 mW cm^{-2} intensity (Omnicure, S2000). Nonperiodic (segmented)

LCE lattices were printed such that each node had a dwell of up to 0.5 s to minimize printing defects.

Thermomechanical Characterization: The deformation of LCE thick films (uniaxially aligned controls, Figure 1e) and homogeneous and heterogeneous triangular lattices as a function of temperature was measured by heating 3D printed samples on a hotplate coated in silicone oil while imaging them from above using a camera (Canon Rebel EOS Ti2) on a white or black-painted (Zynolyte) metal surface. Their temperature was measured by an external thermometer (Cole Parmer). Their normalized actuation length was measured on 3D printed uniaxial thick films with approximate dimensions of $7.5 \times 2 \times 0.25$ mm³ and $18 \times 1 \times 0.5$ mm³ while heating following the same procedure combined with image analysis software (ImageJ). The deformation behavior of each triangular LCE lattice was measured by marking nodes with a red marker (Sarstedt) prior to heating on a silicone oil-coated, white metal surface (Figure S4, Supporting Information). The center of each red dot is determined and tracked using a custom MATLAB image analysis script with preprocessing using ImageJ (Figure S16, Supporting Information). Global deformations in the x direction and y direction are defined by the length between the left and right nodes at the midpoint (row 5) and as the average length between the upper left-upper right nodes line and lower left-lower right nodal line, respectively. To calculate normalized actuation dimensions, their length at each temperature is divided by the initial length under ambient conditions (22 °C). Average normalized aspect ratio is calculated by averaging the aspect ratio of each of three replicates for each type of periodic lattice and dividing by aspect ratio at ambient conditions, where aspect ratio is x/y .

Mechanical properties of 3D printed LCE thick films (uniaxially aligned, Figure 1f) and lattices were performed on a stress-controlled shear rheometer equipped with tensile grips and environmental heating chamber (Discovery HR-20 Hybrid Rheometer, TA Instruments). To measure their Young's modulus, uniaxially aligned films with approximate dimensions of $20 \times 1 \times 0.5$ mm³ were strained 5% while suppressing rotation. Each sample was allowed to reach equilibrium deformation at target temperatures prior to testing, such that the initial bias load was ~ 0 N for each temperature condition and applied stress is not distorted by actuation stress. Their Young's modulus at each temperature measured was determined from the slope of their engineering stress-stretch curve. Stretch was calculated by using the initial length of each temperature condition. Stress was calculated using measured force over the cross-sectional area. The cross-sectional area of uniaxially aligned LCE films is estimated from the length in the stretch direction at each temperature compared to the value at room temperature. For triangular LCE lattices, their cross-sectional area is defined by the cross-sectional area of eight struts, without adjusting for deformation at elevated temperatures. Lattices were strained 7% at each test temperature at constant 100% min^{-1} strain rate.

Modeling: Additional details on the modeling and inverse design of LCE lattices as well as quantitative comparison to experimental data are provided in supporting information (Figures S17 and S18, and Movie S4, Supporting Information).

Supporting Information

Supporting Information is available from the Wiley Online Library or from the author.

Acknowledgements

The authors gratefully acknowledge support from the National Science Foundation through the Harvard MRSEC (DMR-2011754) and the ARO MURI program (W911NF-17-1-03; W911NF-22-1-0219). A. Spielberg was supported by a postdoctoral fellowship from the Defense Advanced Research Projects Agency Information Office Fellowship (HR00112110007). This work made use of the Shared Experimental Facilities supported in part by the Harvard MRSEC, and this work was performed in part at the Harvard University Center for Nanoscale Systems (CNS); a member of the National Nanotechnology Coordinated Infrastructure Network (NNCI),

which is supported by the National Science Foundation under NSF award no. ECCS-2025158. The authors thank N. Colella, R. Telles, J. Muhammad, and C. Baek for helpful discussions.

Conflict of Interest

The authors declare no conflict of interest.

Data Availability Statement

The source code developed for the modeling and inverse-design and inverse design data is available on GitHub at github.com/bertoldi-collab/morphing-lattices. All the experimental data is attached as Supporting Information.

Keywords

active lattices, additive manufacturing, liquid crystal elastomers, shape-morphing

Received: October 15, 2023

Revised: December 9, 2023

Published online:

- [1] K. Liu, F. Hacker, C. Daraio, *Sci. Robot.* **2021**, 6, eabf5116.
- [2] A. Kotikian, C. McMahon, E. C. Davidson, J. M. Muhammad, R. D. Weeks, C. Daraio, J. A. Lewis, *Sci. Robot.* **2019**, 4, eaax7044.
- [3] Q. He, Z. Wang, Y. Wang, A. Minori, M. T. Tolley, S. Cai, *Sci. Adv.* **2019**, 5, eaax5746.
- [4] M. J. Ford, C. P. Ambulo, T. A. Kent, E. J. Markvicka, C. Pan, J. Malen, T. H. Ware, C. Majidi, *Proc. Natl. Acad. Sci. U. S. A.* **2019**, 116, 21438.
- [5] T. H. Ware, M. E. Mcconney, J. J. Wie, V. P. Tondiglia, T. J. White, *Science* **2015**, 347, 982.
- [6] J. Küpfer, H. Finkelmann, *Makromol. Chem., Rapid Commun.* **1991**, 12, 717.
- [7] H. Aharoni, Y. Xia, X. Zhang, R. D. Kamien, S. Yang, *Proc. Natl. Acad. Sci. U. S. A.* **2018**, 115, 7206.
- [8] M. Prévôt, S. Ustunel, E. Hegmann, *Materials* **2018**, 11, 377.
- [9] Y. Wang, R. Yin, L. Jin, M. Liu, Y. Gao, J. Raney, S. Yang, *Adv. Funct. Mater.* **2023**, 33, 2210614.
- [10] A. W. Hauser, D. Liu, K. C. Bryson, R. C. Hayward, D. J. Broer, *Macromolecules* **2016**, 49, 1575.
- [11] S. Li, B. Deng, A. Grinthal, A. Schneider-Yamamura, J. Kang, R. S. Martens, C. T. Zhang, J. Li, S. Yu, K. Bertoldi, J. Aizenberg, *Nature* **2021**, 592, 386.
- [12] K. Kim, Y. Guo, J. Bae, S. Choi, H. Y. Song, S. Park, K. Hyun, S.-K. Ahn, *Small* **2021**, 17, 2100910.
- [13] T. J. White, D. J. Broer, *Nat. Mater.* **2015**, 14, 1087.
- [14] S. W. Ula, N. A. Traugutt, R. H. Volpe, R. R. Patel, K. Yu, C. M. Yakacki, *Liq. Cryst. Rev.* **2018**, 6, 78.
- [15] B. A. Kowalski, V. P. Tondiglia, T. Guin, T. J. White, *Soft Matter* **2017**, 13, 4335.
- [16] S. Li, G. Librandi, Y. Yao, A. J. Richard, A. Schneider-Yamamura, J. Aizenberg, K. Bertoldi, *Adv. Mater.* **2021**, 33, 2105024.
- [17] B. Ni, G. Liu, M. Zhang, M. Tatoulian, P. Keller, M.-H. Li, *ACS Appl. Mater. Interfaces* **2021**, 13, 54439.
- [18] C. P. Ambulo, J. J. Burroughs, J. M. Boothby, H. Kim, M. R. Shankar, T. H. Ware, *ACS Appl. Mater. Interfaces* **2017**, 9, 37332.
- [19] A. Kotikian, R. L. Truby, J. W. Boley, T. J. White, J. A. Lewis, *Adv. Mater.* **2018**, 30, 1706164.
- [20] N. A. Traugutt, D. Mistry, C. Luo, K. Yu, Q. Ge, C. M. Yakacki, *Adv. Mater.* **2020**, 32, 2000797.
- [21] Z. Wang, Z. Wang, Y. Zheng, Q. He, Y. Wang, S. Cai, *Sci. Adv.* **2020**, 6, eaba9319.
- [22] X. Peng, S. Wu, X. Sun, L. Yue, S. M. Montgomery, F. Demoly, K. Zhou, R. R. Zhao, H. J. Qi, *Adv. Mater.* **2022**, 34, 2204890.
- [23] C. Yuan, D. J. Roach, C. K. Dunn, Q. Mu, X. Kuang, C. M. Yakacki, T. J. Wang, K. Yu, H. J. Qi, *Soft Matter* **2017**, 13, 5558.
- [24] A. Kotikian, J. M. Morales, A. Lu, J. Mueller, Z. S. Davidson, J. W. Boley, J. A. Lewis, *Adv. Mater.* **2021**, 33, 2101814.
- [25] M. R. Vinciguerra, D. K. Patel, W. Zu, M. Tavakoli, C. Majidi, L. Yao, *ACS Appl. Mater. Interfaces* **2023**, 15, 24777.
- [26] D. J. Roach, C. Yuan, X. Kuang, V. C.-F. Li, P. Blake, M. L. Romero, I. Hammel, K. Yu, H. J. Qi, *ACS Appl. Mater. Interfaces* **2019**, 11, 19514.
- [27] J. Sun, W. Liao, Z. Yang, *Adv. Mater.* **2023**, 35, 2302706.
- [28] J. M. Mccracken, B. R. Donovan, K. M. Lynch, T. J. White, *Adv. Funct. Mater.* **2021**, 31, 2100564.
- [29] G. E. Bauman, J. M. Mccracken, T. J. White, *Angew. Chem., Int. Ed.* **2022**, 61, e202202577.
- [30] M. O. Saed, C. P. Ambulo, H. Kim, R. De, V. Raval, K. Searles, D. A. Siddiqui, J. M. O. Cue, M. C. Stefan, M. R. Shankar, T. H. Ware, **2019**, 29, 1806412.
- [31] H. Finkelmann, A. Greve, M. Warner, *Eur. Phys. J. E* **2001**, 5, 281.
- [32] R. D. Weeks, R. L. Truby, S. G. M. Uzel, J. A. Lewis, *Adv. Mater.* **2023**, 35, 2206958.
- [33] M. P. Bendsøe, O. Sigmund, *Arch. of Appl. Mech.* **1999**, 69, 635.
- [34] K. Svanberg, *Int. J. Numer. Meth. Eng.* **1987**, 24, 359.

ADVANCED MATERIALS

Supporting Information

for *Adv. Mater.*, DOI 10.1002/adma.202310743

Liquid Crystal Elastomer Lattices with Thermally Programmable Deformation via
Multi-Material 3D Printing

*Arda Kotikian, Audrey A. Watkins, Giovanni Bordiga, Andrew Spielberg, Zoey S. Davidson, Katia Bertoldi and Jennifer A. Lewis**

Supporting Information

Liquid crystal elastomer lattices with thermally programable deformation via multi-material 3D printing

Arda Kotikian, Audrey A. Watkins, Giovanni Bordiga, Andrew Spielberg, Zoey S. Davidson, Katia Bertoldi, and Jennifer A. Lewis**

Modeling

The response of the LCE lattices is modeled via a network of thermo-elastic springs with temperature-dependent material properties^[1] and represents a good compromise between simplicity and accuracy for modeling lattices of 1D elements.

By denoting the stretch as λ , the strain energy of each strut is assumed to be:

$$\psi = \frac{1}{2} E(T) A_0 l_0 \left(\frac{\lambda}{1 + \alpha [\lambda_T(T) - 1]} - 1 \right)^2$$
 $E(T)$ and $\lambda_T(T)$ are the Young's modulus and the thermal stretch (actuation) as a function of the current temperature T of the LCE material, $A_0 = 0.0625 \text{ mm}^2$ or 0.0313 mm^2 and $l_0 = 2.9 \text{ mm}$ are the cross-sectional area and length of the strut in the nematic phase at room temperature ($T = T_0 = 22^\circ\text{C}$). We introduce a fitting parameter, α , to account for lower director orientational order at each node within the printed periodic LCE lattices and we chose $\alpha = 0.7$ and $\alpha = 0.8$ for LTNI and HTNI LCE, respectively. The experimentally measured properties $E(T)$ and $\lambda_T(T)$ are assigned to each strut based on the LCE composition (i.e., LTNI or HTNI). Note, we account for the temperature dependence of the Young's modulus in the strain energy function and the thermal actuation, unlike Daraio and colleagues, who only accounted for the latter dependency.^[1]

where $E(T)$ and $\lambda_T(T)$ are the Young's modulus and the thermal stretch (actuation) as a function of the current temperature T of the LCE material, $A_0 = 0.0625 \text{ mm}^2$ or 0.0313 mm^2 and $l_0 = 2.9 \text{ mm}$ are the cross-sectional area and length of the strut in the nematic phase at room temperature ($T = T_0 = 22^\circ\text{C}$). We introduce a fitting parameter, α , to account for lower director orientational order at each node within the printed periodic LCE lattices and we chose $\alpha = 0.7$ and $\alpha = 0.8$ for LTNI and HTNI LCE, respectively. The experimentally measured properties $E(T)$ and $\lambda_T(T)$ are assigned to each strut based on the LCE composition (i.e., LTNI or HTNI). Note, we

account for the temperature dependence of the Young's modulus in the strain energy function and the thermal actuation.

The total strain energy of the lattice Ψ is obtained by summing ψ_{strut} over all the struts of the network and all nodes are modeled as perfect hinges. The elastic forces acting on nodes of the lattice are given by $F_e = -\partial\Psi(u)/\partial u$, where u is the vector describing the nodal displacements. To simulate LCE lattice response to a given temperature evolution $T(t)$, we adopt a dynamic approach in which the state vector $\{u, v\}$ is integrated over time by solving the following equations of motion:

$$du/dt = v, dv/dt = (F_e - cv)/m,$$

where c is a viscous damping coefficient (0.03Mg/s) and m is the nodal inertia. In all simulations, the temperature is assumed to evolve linearly from the reference temperature $T(t) = T_0 + (T_f - T_0)t/t_f$ with $t \in [0, t_f]$. The parameters t_f , c , and m are chosen to simulate a quasi-static process. We use $t_f = 9000s$ for periodic lattices and the meandering lattice (Figure 5b) and $t_f = 36000s$ for the bending lattice (Figure 5a) due to its length. Compared to periodic lattices, the nonperiodic lattice print path is non-optimized, so we use fitting parameters $\alpha = 0.6$ and $\alpha = 0.8$ in for the LTNI and HTNI LCE strain inputs, respectively, to account for the lower director orientational order at each node within these lattices. The equations of motion are integrated using a Runge-Kutta 45 method with an adaptive step size.

We have developed a computational model written in Python to automate the generation of the lattice geometry, material model, equations of motion, and numerical integration (github.com/bertoldi-collab/morphing-lattices). The code leverages the JAX library for the automatic derivation of the equations of motion and fast integration via just-in-time compilation to XLA code.^[2-5]

Inverse design framework

As part of this study, we developed an inverse-design framework for identifying multi-material LCE lattices that morph into multiple target shape configurations upon monotonic heating. Towards this end, we set the distribution of LTNI and HTNI struts to be our design variable. For

any given reference lattice configuration at room temperature, we introduce two target configurations at two different temperatures T_1 and T_2 defined by an ordered set of N_{target} points in 2D space that can be represented by two target vectors $y^{(1)} \in \mathfrak{R}^{2 \times N_{target}}$, $y^{(2)} \in \mathfrak{R}^{2 \times N_{target}}$. A scale-invariant cost function J is introduced to measure the distance between the coordinates of the target nodes of the lattice configuration $x(T_i)$ at the target temperature T_i and the target configuration $y^{(i)}$

$$J_i = \left\| \frac{x(T_i)}{l(x(T_i))} - \frac{y^{(i)}}{l(y^{(i)})} \right\|_2$$

where the $l(\cdot)$ function simply computes the length of the polyline of a set of points (used to make J_i scale-invariant) and $\|\cdot\|_2$ denotes the standard l^2 -norm. The target nodes, $y^{(i)}$, for the three inverse designed lattices are highlighted in green and purple in Figure 5c-d, Figure S19, and Movie S4. To identify the best material distribution for a given lattice to reach its target configuration at a defined temperature, we solved the following multi-objective optimization problem:

$$\min (w_1 J_1 + w_2 J_2)$$

where $w_1 \in [0,1]$ and $w_2 = 1 - w_1$ are weights adjusted to find the best equi-performance design (i.e. $J_1 \approx J_2$). Notably, this inverse-design problem is a discrete optimization in the space of binary material distribution with dimension $2^{N_{struts}}$, which becomes quickly computationally intractable unless the lattice is very small (small number of struts). Hence, we converted this discrete optimization problem into a continuous one in the N_{struts} -dimensional space. Akin to the well-known SIMP method,^[6] we considered each strut to be made of a ‘blended’ material with thermo-elastic properties interpolated between LTNI and HTNI. Specifically, a phase variable $z \in [0,1]$ is introduced on each strut so that the Young’s modulus and the thermal stretch are given by:

$$\begin{aligned} E &= E_{HTNI} + (E_{LTNI} - E_{HTNI}) z^p \\ \lambda_T &= \lambda_{T,HTNI} + (\lambda_{T,LTNI} - \lambda_{T,HTNI}) z^p \end{aligned}$$

where the penalization factor $p = 3$ is selected to penalize intermediate phase values thus favoring binary solutions. Since the optimization problem has now been made continuous in the phase variable $z \in [0,1]^{N_{struts}}$, we can leverage the differentiability of our simulations and minimize the cost function using a gradient-based strategy, which is efficient in large design spaces. In particular, we adopt the Method of Moving Asymptotes (MMA)^[7] to identify the optimal value for the phase variable in each strut and then threshold the solution to be only LTNI ($z = 1$) and HTNI ($z = 0$) material. This ensures printability of the discovered optimal material distribution.

This minimization procedure is repeated by sweeping the weights $w_1 \in [0,1]$ and $w_2 = 1 - w_1$ to sample the Pareto front of the multi-objective problem – from which an optimal design is then selected. The result of this optimization sweep is reported in Figure S20 showing the sampled Pareto front for the multi-target designs shown in Figure 5d and S19. The emerging Pareto front reveals the trade-off inherent in the design of multi-target shape-morphing lattices and allows the selection of optimal designs with different performances.

We also point out that the simplicity of the discrete model and the JAX-based implementation allows the optimization to be fast enough to be run on a consumer-grade laptop in a matter of minutes. All code developed for this work can be found at github.com/bertoldi-collab/morphing-lattices.

- [1] K. Liu, F. Hacker, C. Daraio, *Sci Robot* **2021**, 6, eabf5116.
- [2] Bradbury, J., Frostig, R., Hawkins, P., Johnson, M.J., Leary, C., Maclaurin, D., Necula, G., Paszke, A., VanderPlas, J., Wanderman-Milne, S. and Zhang, Q., **2018**. JAX: composable transformations of Python+ NumPy programs.
- [3] M. Minkov, I. A. D. Williamson, L. C. Andreani, D. Gerace, B. Lou, A. Y. Song, T. W. Hughes, S. Fan, *ACS Photonics* **2020**, 7, 1729.
- [4] C. P. Goodrich, E. M. King, S. S. Schoenholz, E. D. Cubuk, M. P. Brenner, *Proceedings of the National Academy of Sciences* **2021**, 118, e2024083118.
- [5] S. S. Schoenholz, E. D. Cubuk, *Adv Neural Inf Process Syst* **2019**, 33, 11428.
- [6] Bendsøe, M. P., & Sigmund, O. *Archive of applied mechanics* **1999**, 69, 635.
- [7] Svanberg, K. *International journal for numerical methods in engineering* **1987**, 24(2), 359-373.

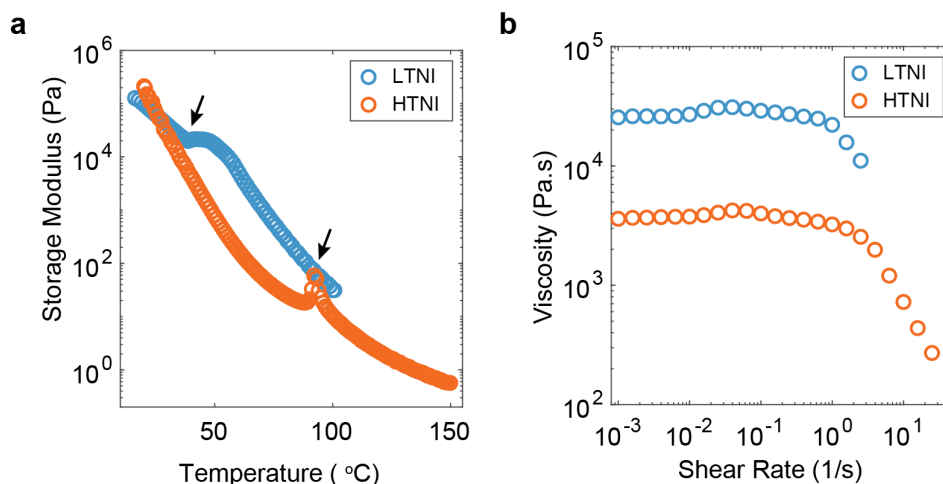


Figure S1. LCE ink rheology. a) Temperature sweep of LTNI (blue) and HTNI (orange) inks at 1Hz. The T_{NI} of the LTNI ink is approximately 38°C, and T_{NI} of the HTNI ink is approximately 92°C and marked with arrows. b) Apparent viscosity as a function of shear rate for LTNI ink (blue) at 31°C and HTNI ink (orange) at 50°C.

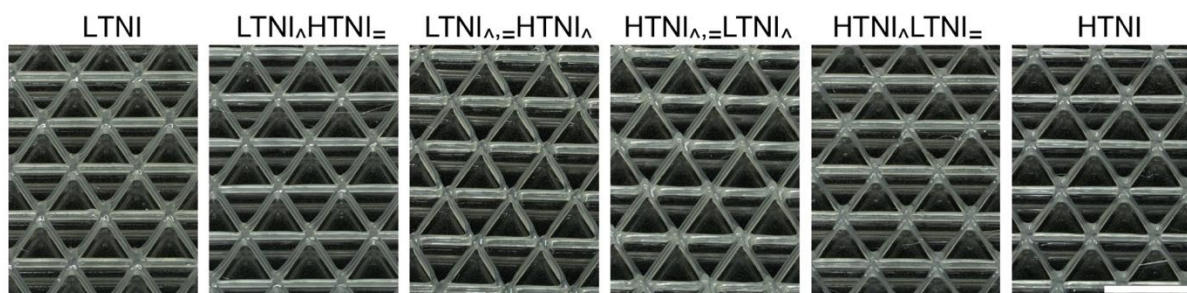


Figure S2. Optical images (tilted view) of triangular LCE lattices of varying unit cell composition (scale bar = 5 mm).

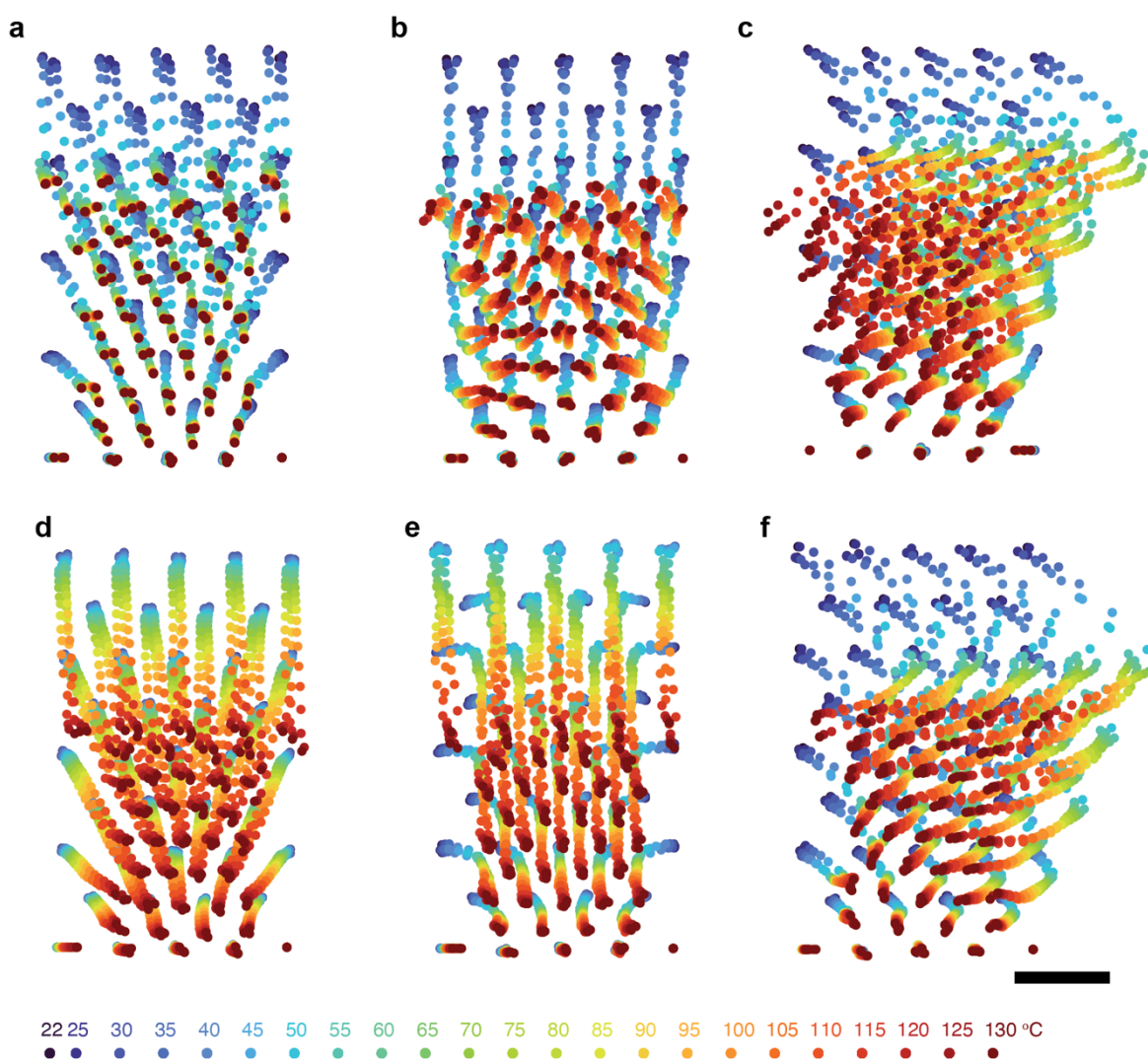


Figure S3. Deformation response of homogeneous and heterogeneous LCE lattices: a) LTNI lattices, b) LTNI \wedge HTNI \neg lattices, c) LTNI \wedge =HTNI \wedge lattices, d) HTNI lattices, e) HTNI \wedge LTNI \neg lattices, and f) HTNI \wedge =LTNI \wedge lattices, where dots depict node locations as a function of temperatures. Dots from $n = 3$ samples are overlaid for each subfigure (scale bar = 5 mm).

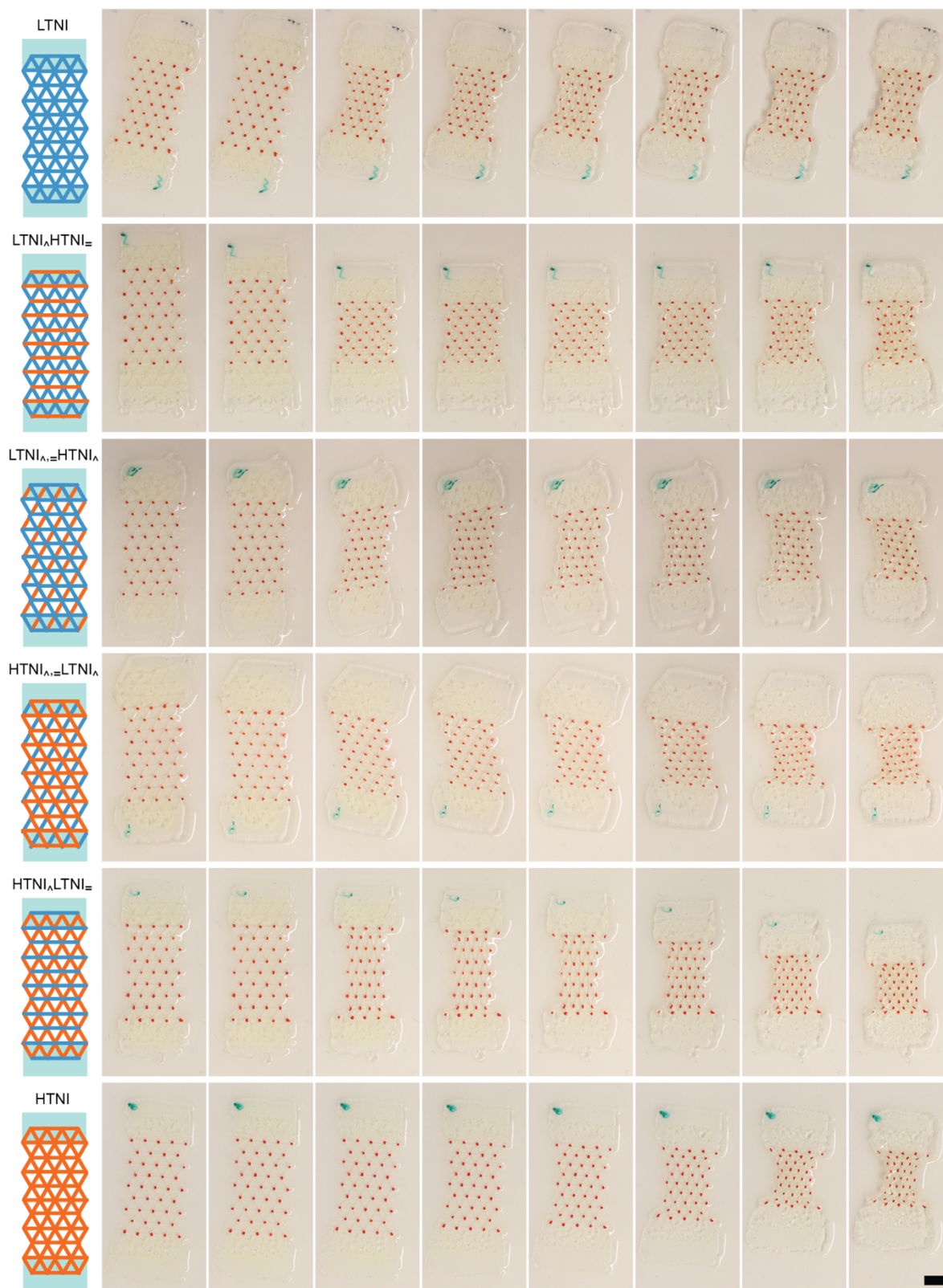


Figure S4. Deformation response of representative LCE lattices with marked nodes (red) at 22 °C, 40 °C, 55 °C, 70 °C, 85 °C, 100 °C, 115 °C, and 130 °C from left to right (scale bar = 5 mm).

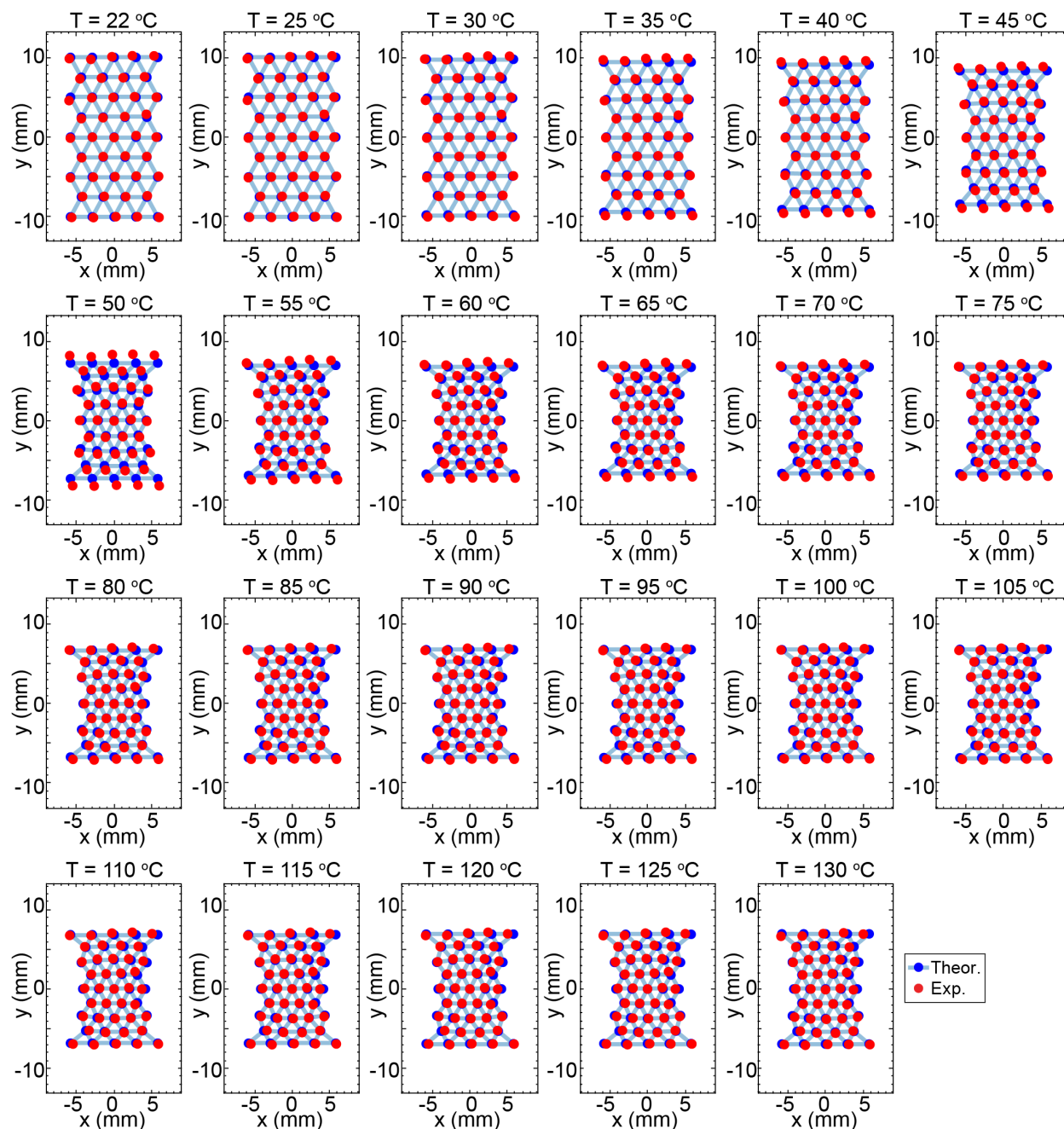


Figure S5. Comparison of the experimentally observed node locations (red) and their predicted deformation response (blue) for a representative LTNI lattice at discrete temperatures.

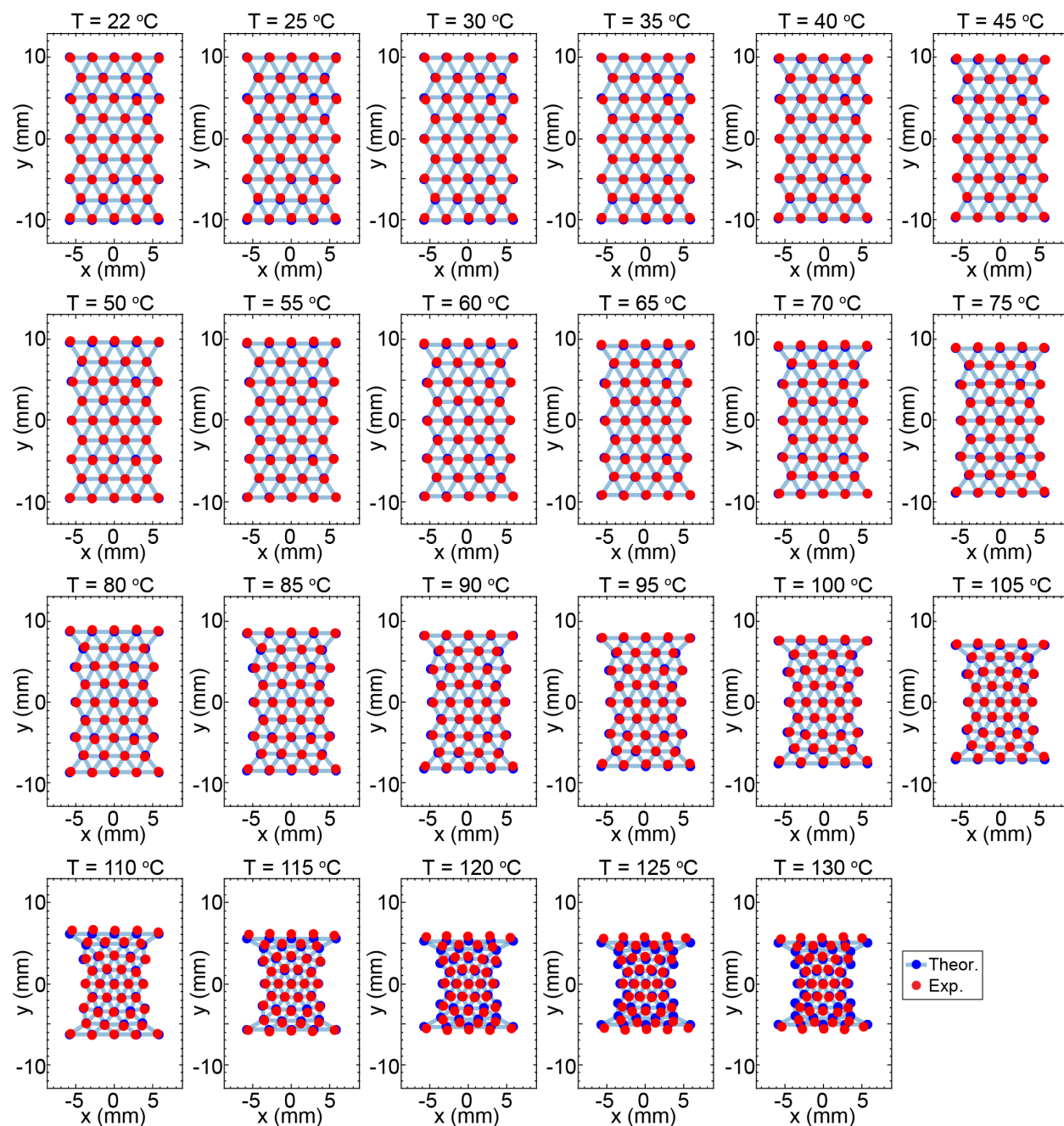


Figure S6. Comparison of the experimentally observed node locations (red) and their predicted deformation response (blue) for a representative HTNI lattice at discrete temperatures.

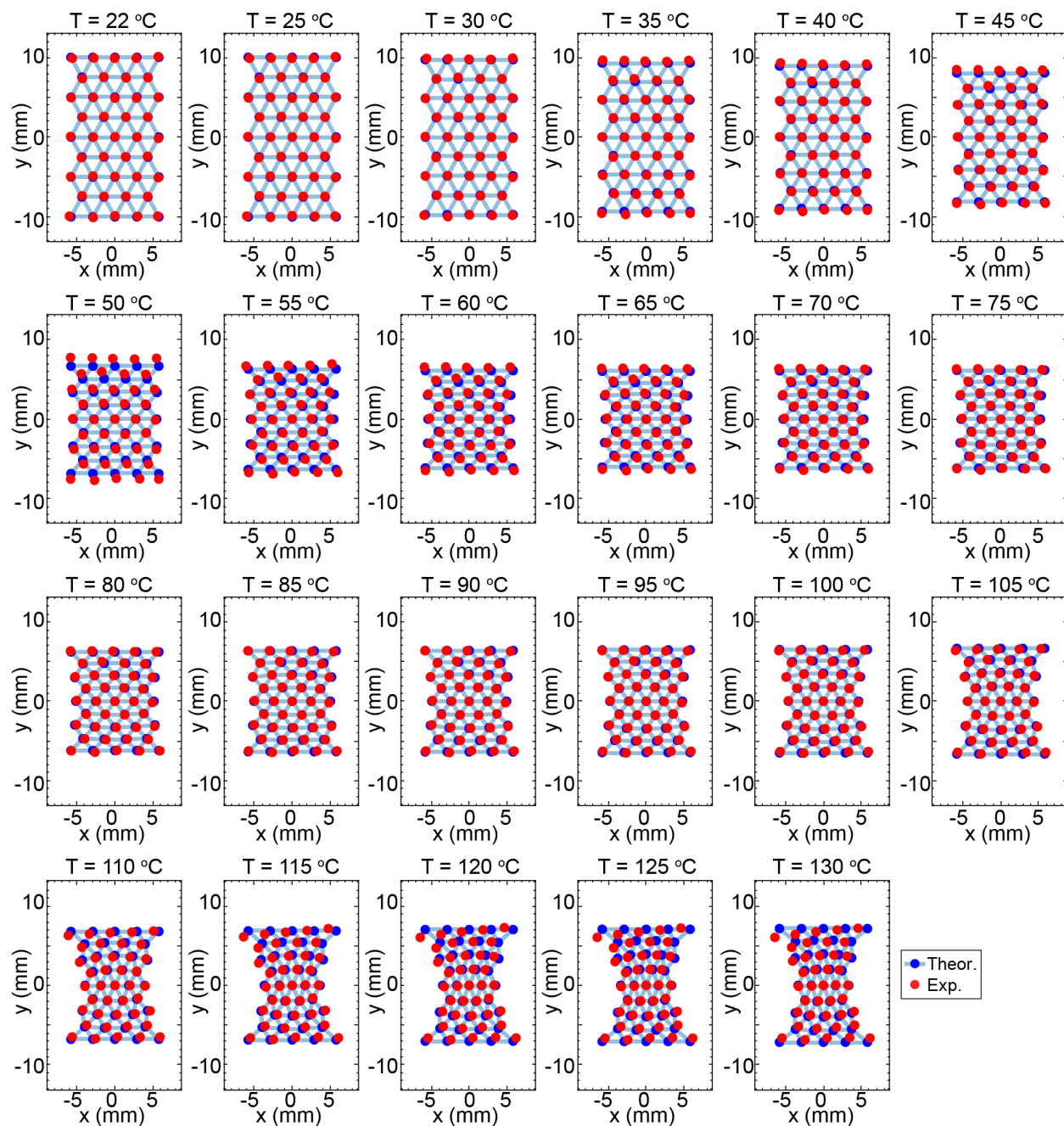


Figure S7. Comparison of the experimentally observed node locations (red) and their predicted deformation response (blue) for a representative LTNI-HTNI lattice at discrete temperatures.

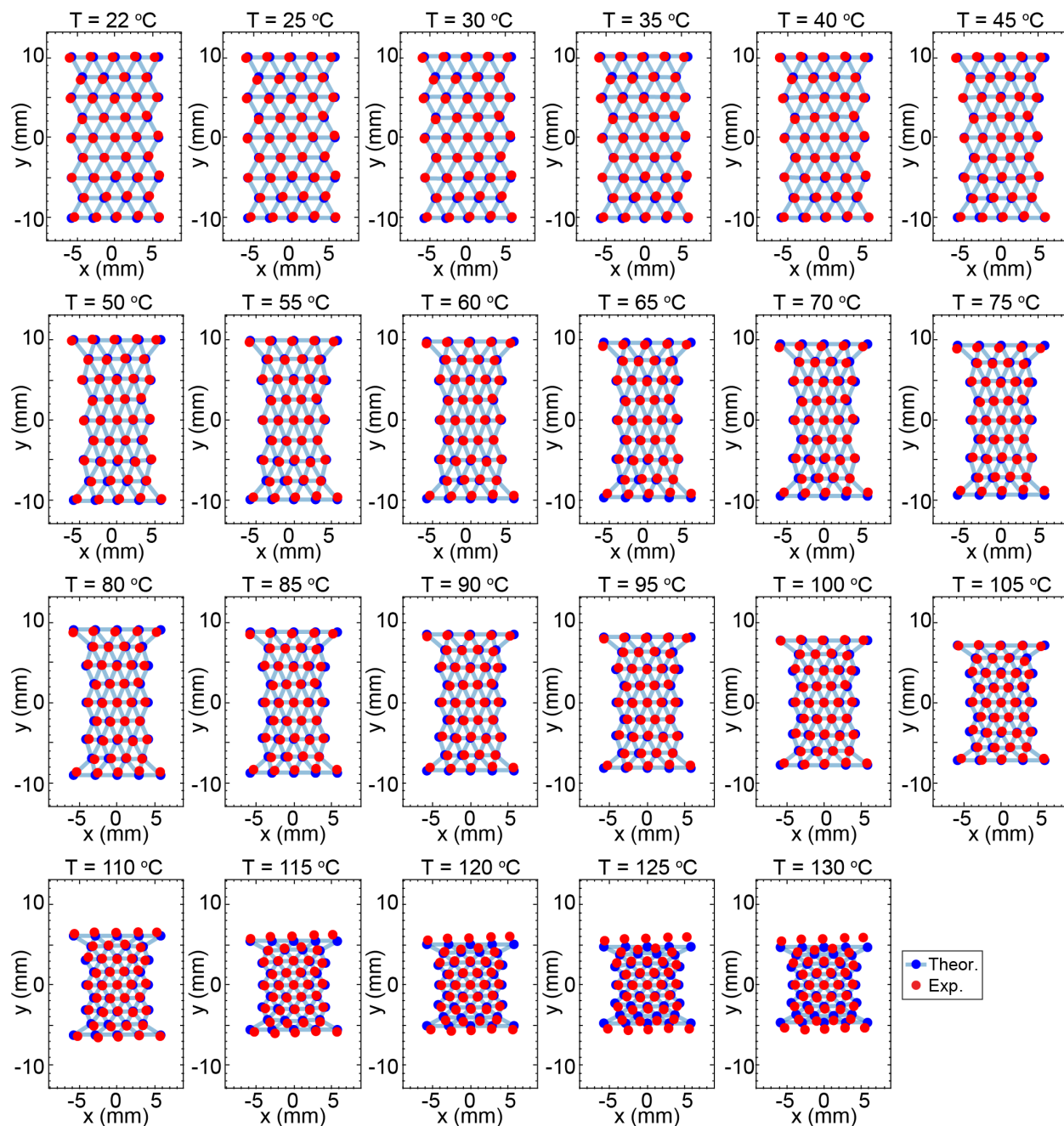


Figure S8. Comparison of the experimentally observed node locations (red) and their predicted deformation response (blue) for a representative HTNI-LTNI lattice at discrete temperatures.

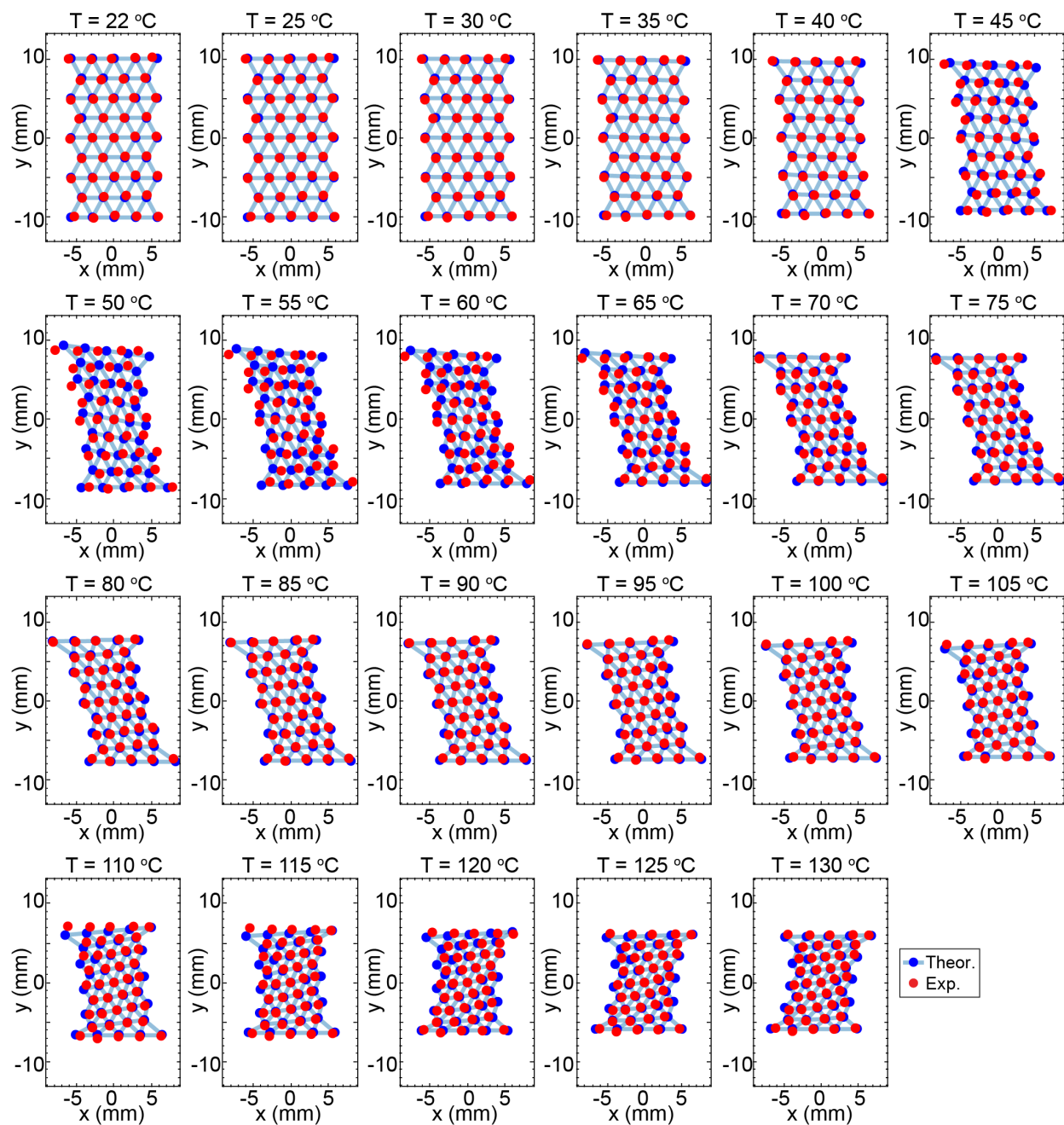


Figure S9. Comparison of the experimentally observed node locations (red) and their predicted deformation response (blue) for a representative $\text{LTNI}_{1-x}\text{HTNI}_x$ lattice at discrete temperatures.

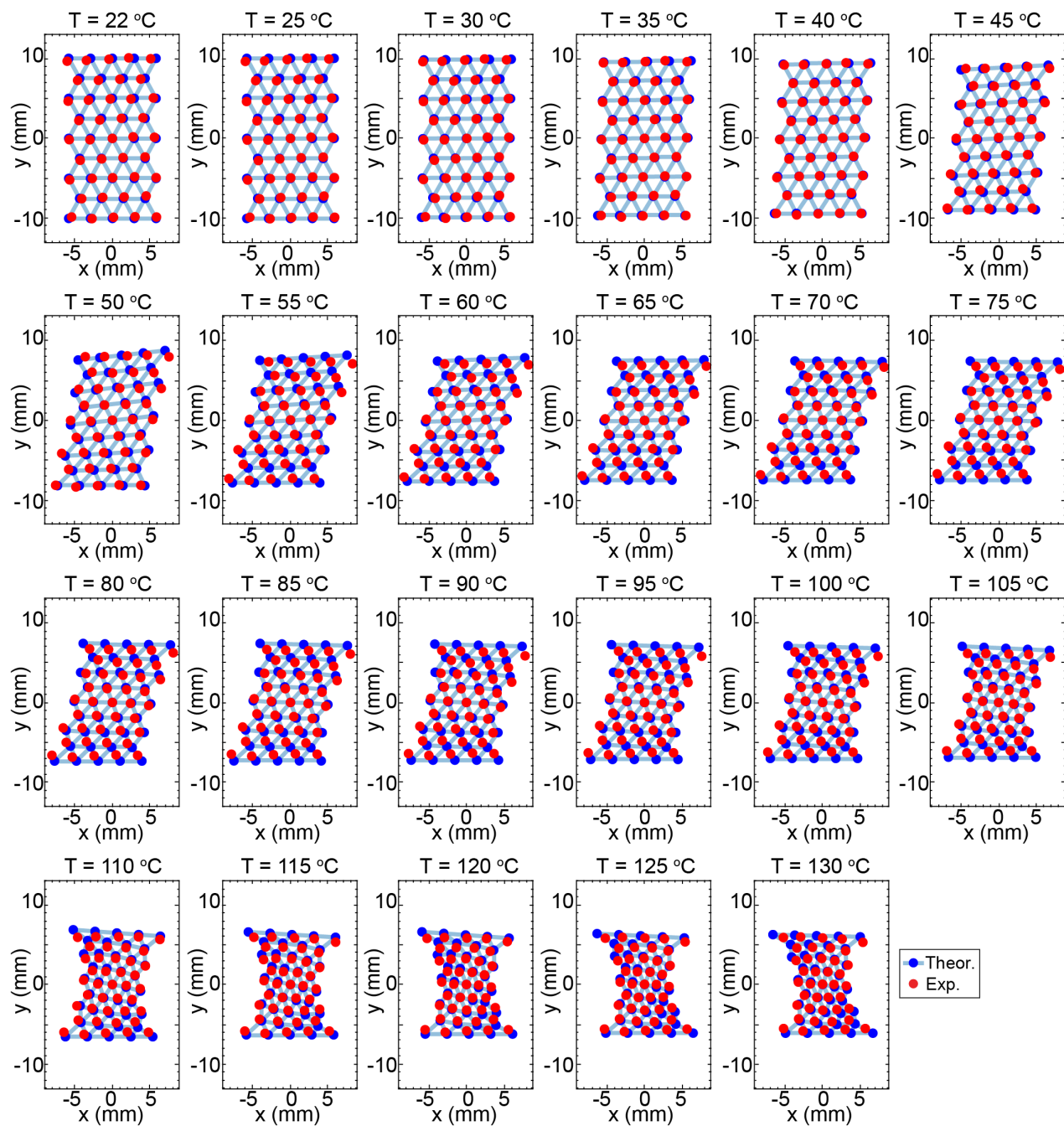


Figure S10. Comparison of the experimentally observed node locations (red) and their predicted deformation response (blue) for a representative HTNI_{1-x}LTNI_x lattice at discrete temperatures.

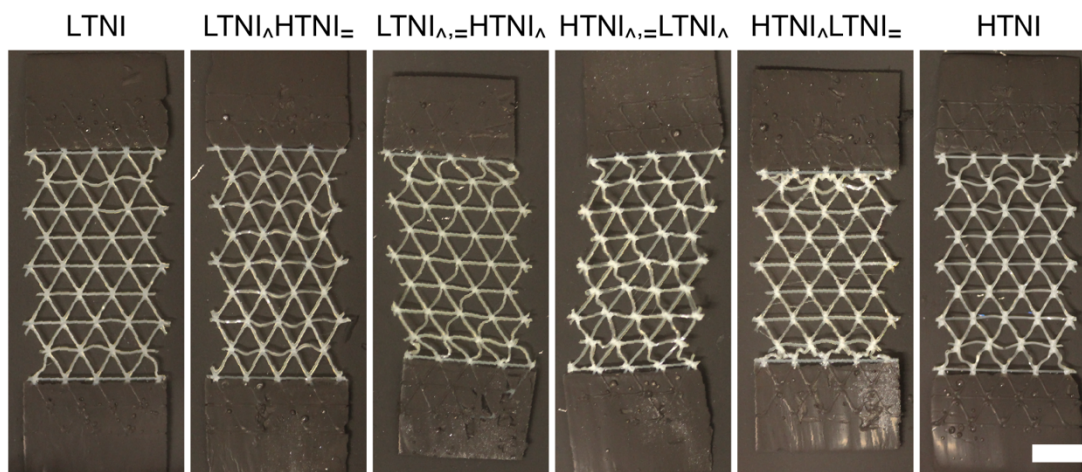


Figure S11. Optical images of triangular LCE lattices of varying until cell composition and topology after heating above 130°C and cooling to room temperature (scale bar = 5 mm).

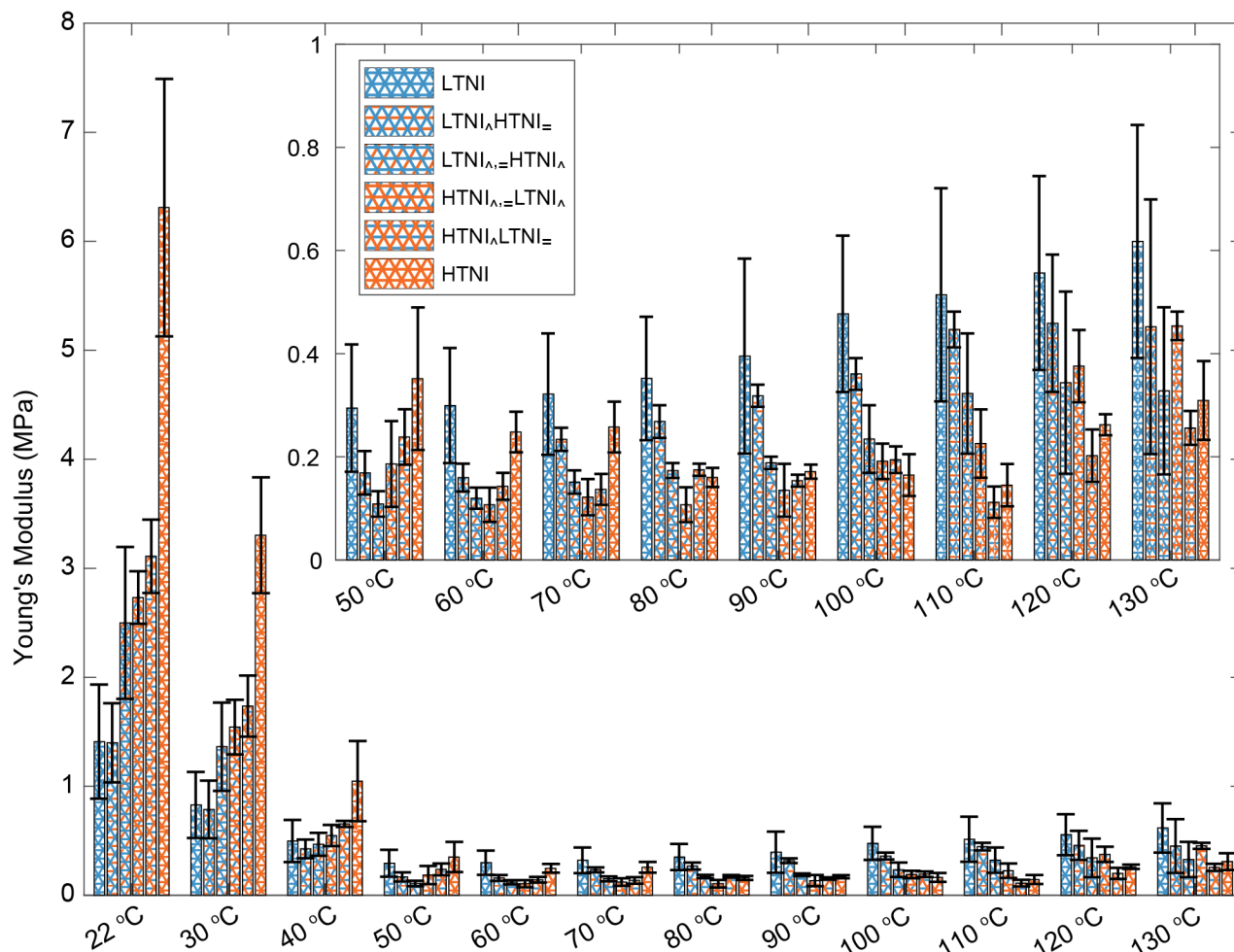


Figure S12. Young's modulus measured as a function of temperature for homogeneous and heterogeneous triangular LCE lattices (LTNI, LTNI \wedge HTNI \equiv , LTNI \wedge =HTNI \wedge , HTNI \wedge =LTNI \wedge , HTNI \wedge LTNI \equiv , and HTNI lattices shown from left to right). Inset provides a magnified view over the temperature values from 50-130°C. Error bars indicate standard deviation (n=3).

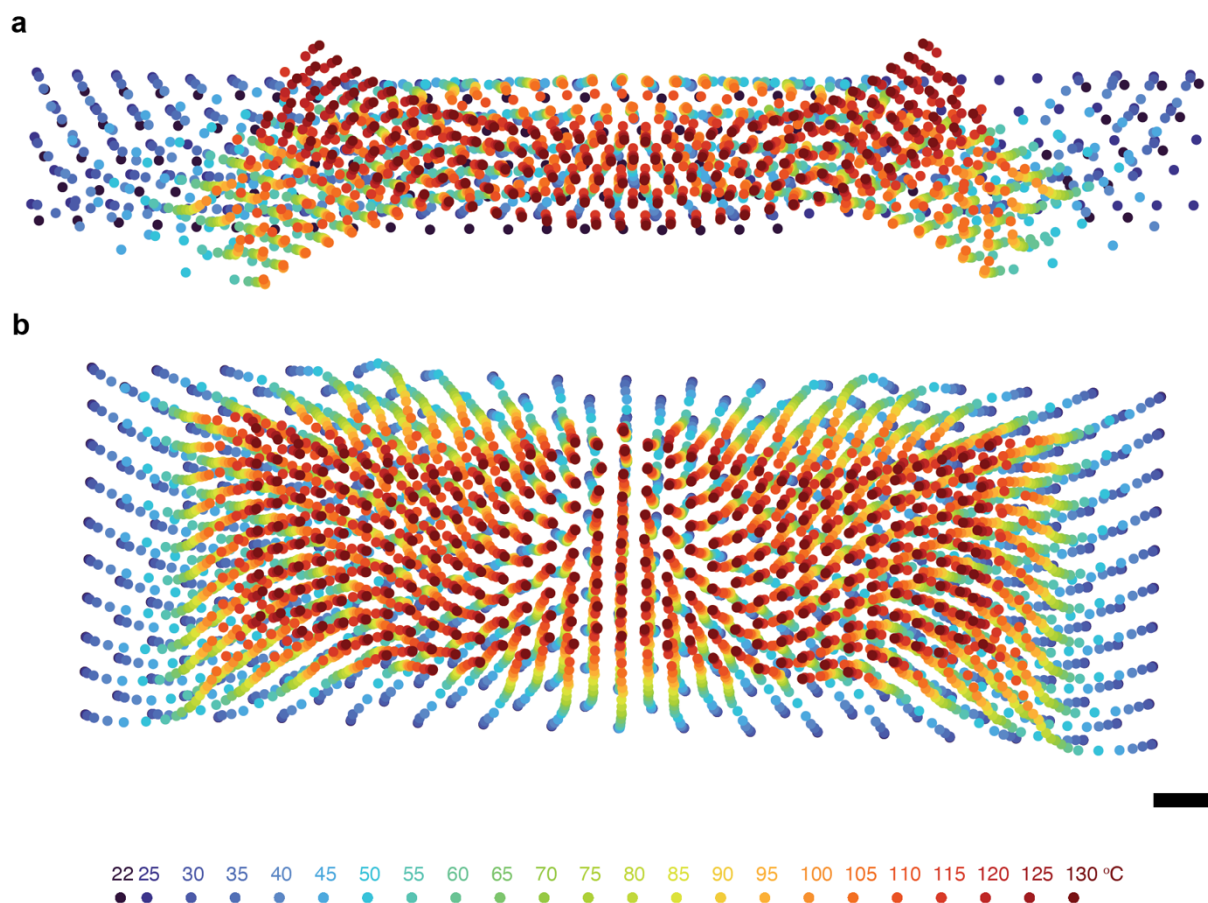


Figure S13. Deformation response of segmented LCE lattices composed of a) HTNI-LTNI bilayer design and b) 4-segment, non-periodic HTNI-LTNI lattice, where dots represent experimentally determined node locations as a function of temperatures (scale bar = 5 mm).

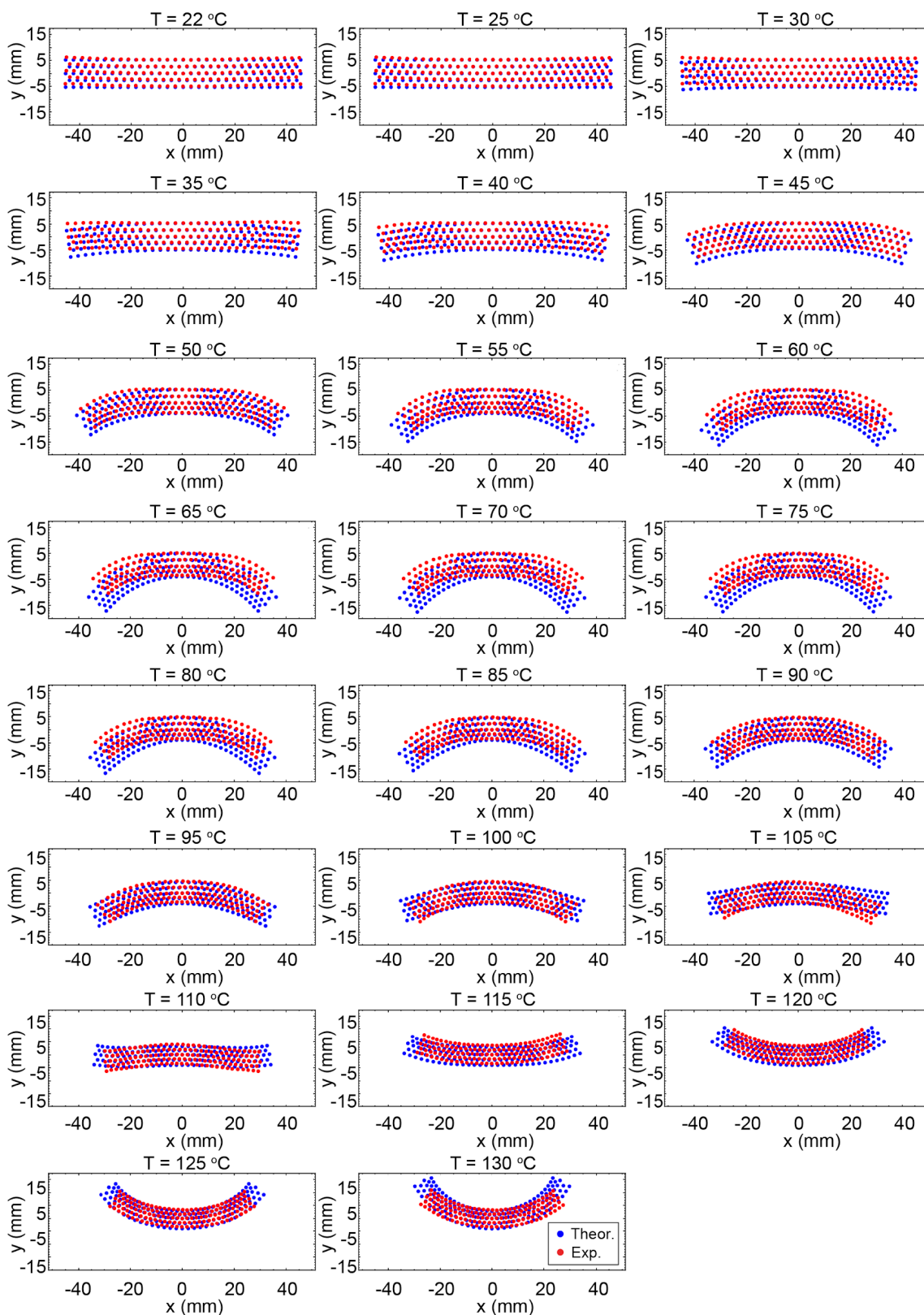


Figure S14. Comparison of the experimentally observed node locations (red) and their predicted deformation response (blue) for a bilayer HTNI-LTNI lattice that bends as a function of temperature.

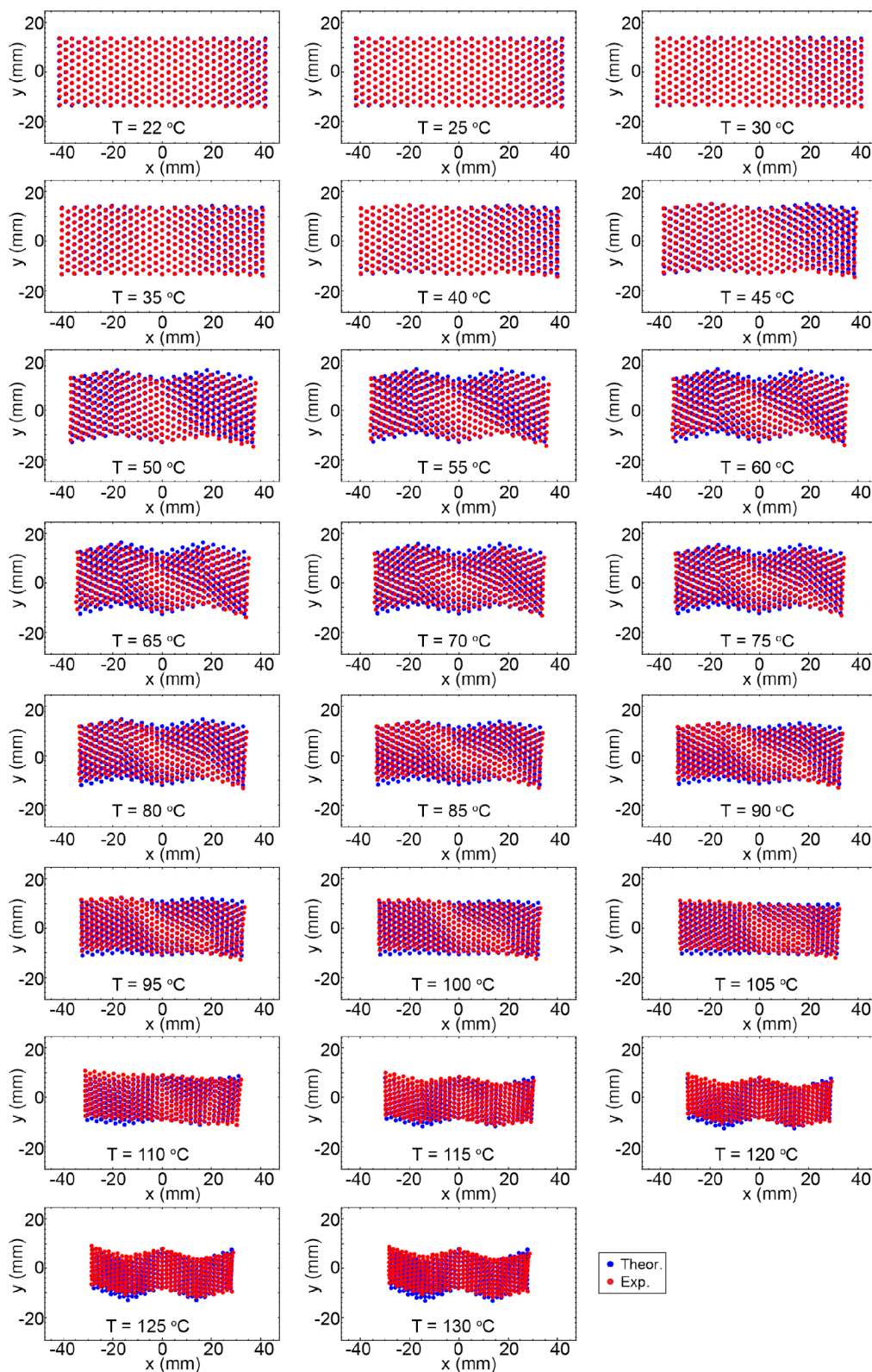


Figure S15. Comparison of experimentally observed node locations (red) and predicted deformation response (blue) for a 4-segment HTNI-LTNI lattice that shape morphs into an accordion-like configuration as a function of temperature.

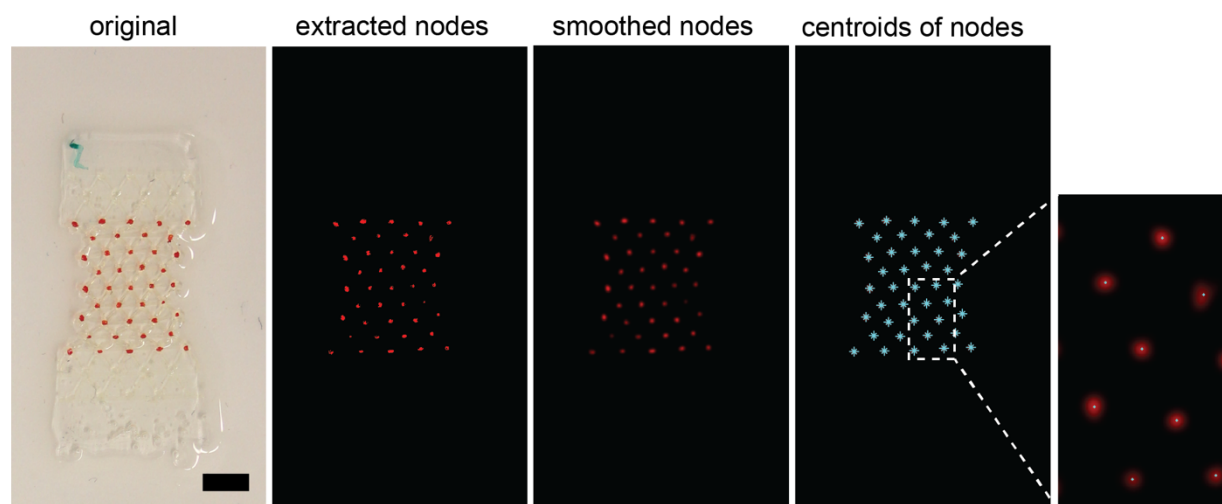


Figure S16. Image processing pipeline for determining node locations as a function of temperature for all LCE lattices tested. [Note: The sequence shown is acquired for a $\text{LTNI}^{\wedge}\text{HTNI}$ lattice at 105 °C.] (scale bar = 5 mm).

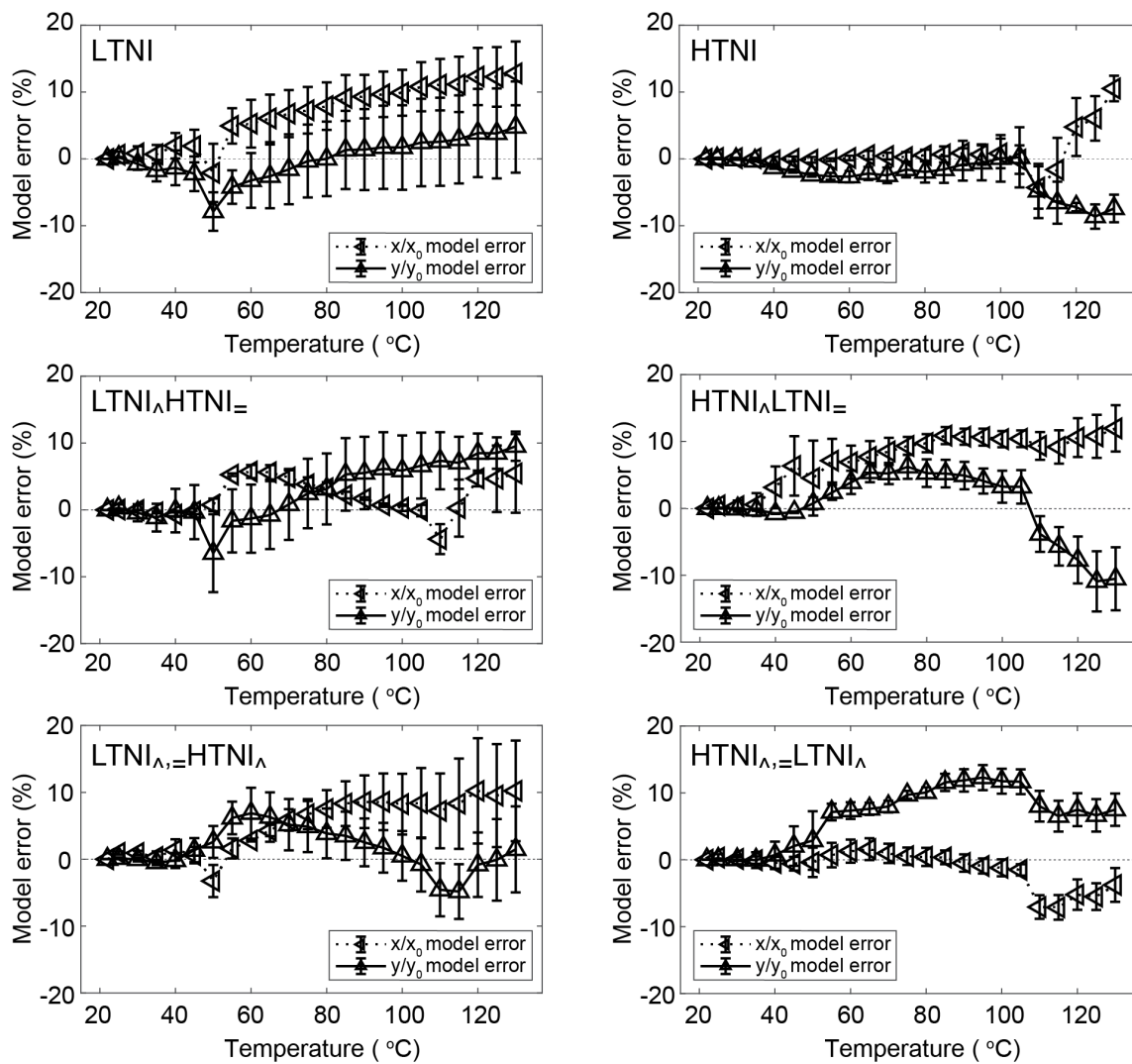


Figure S17. Model error associated with predicted global normalized dimensions x/x_0 and y/y_0 for triangular LCE lattices of varying unit cell composition and topology as a function of temperature. Error bars indicate standard deviation (n=3).

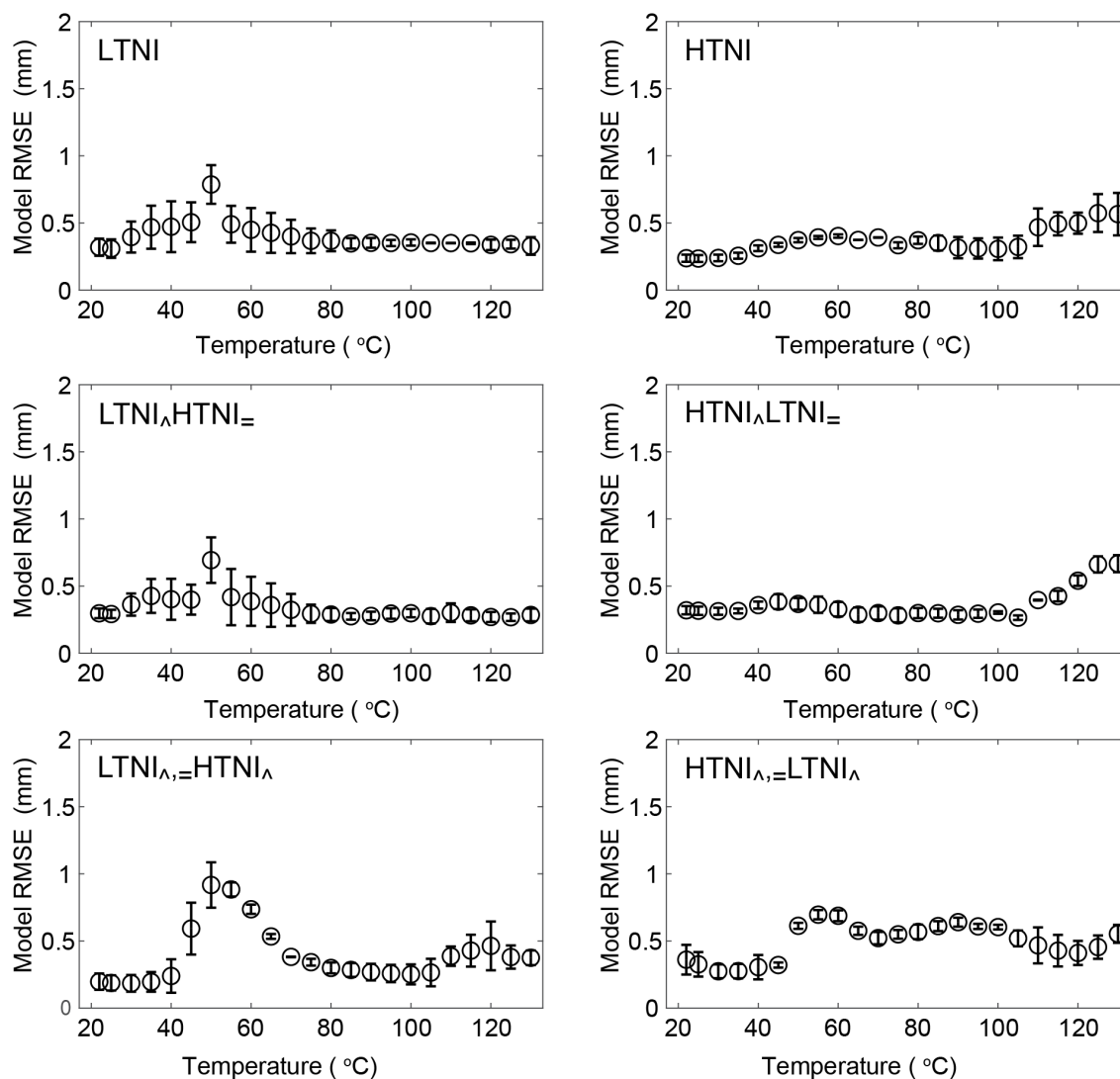


Figure S18. Average root mean square error of modeled lattice nodes compared to their experimentally determined node positions for triangular LCE lattices of varying unit cell composition and topology as a function of temperature. Error bars indicate standard deviation (n=3).

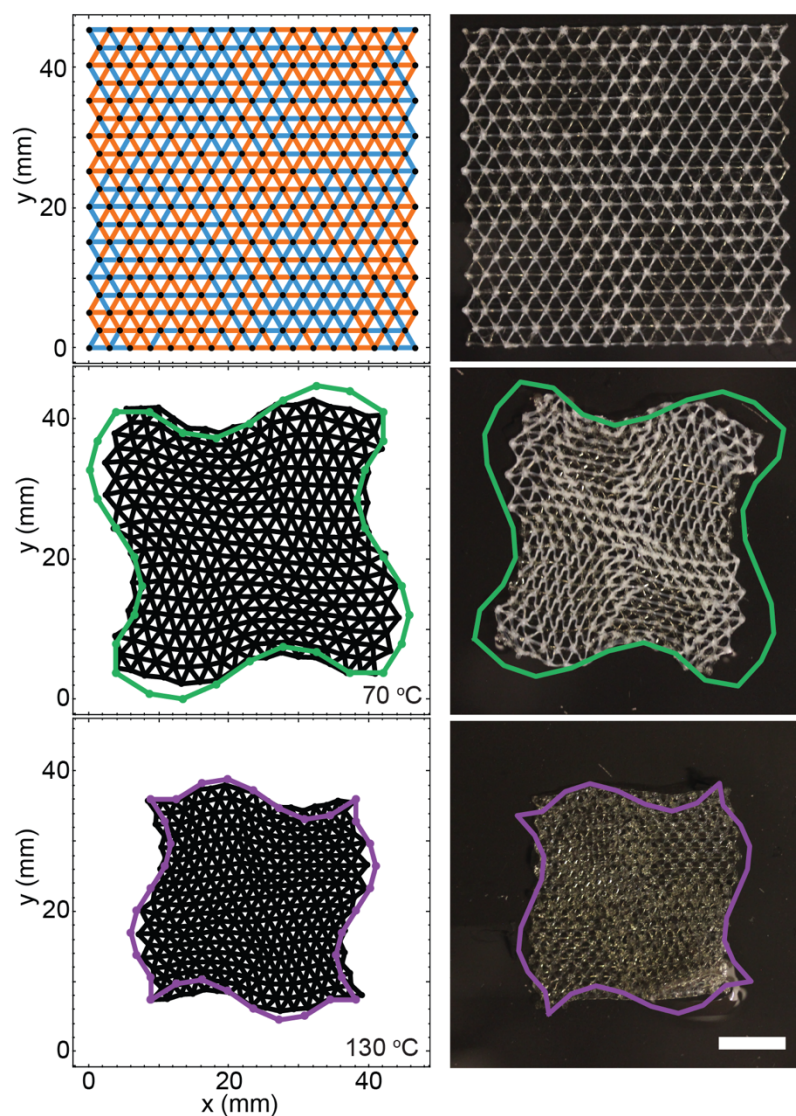


Figure S19. Inverse design of LCE lattices. Simulated inverse designed topology composed of LTNI (blue) and HTNI (orange) LCE struts to achieve green and purple configurations at 70 and 130 °C, respectively, where black denotes modeled deformation and the corresponding experimental data for an alternating shape lattice (scale bars = 10 mm).

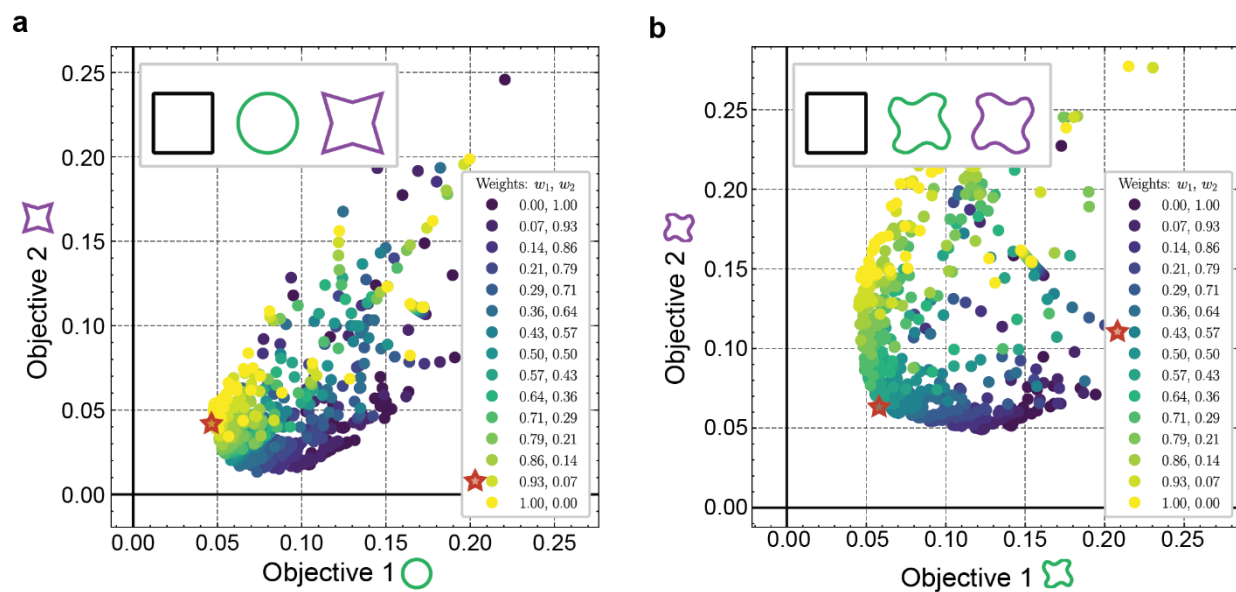


Figure S20. Pareto front sampling for multi-target shape morphing lattices. All designs explored during optimization are reported as dots colored according to the weights combination used in the multi-objective problem. The designs marked with a red star are selected as the best equi-performance designs and have been fabricated and tested.